



JÖNKÖPING UNIVERSITY  
*School of Engineering*

Doctoral Thesis

# **Multiscale Constitutive Modeling of Heterogeneous Engineering Materials**

Johan Jansson

Jönköping University  
School of Engineering  
Dissertation Series No. 065 • 2021





JÖNKÖPING UNIVERSITY

*School of Engineering*

Doctoral Thesis

# **Multiscale Constitutive Modeling of Heterogeneous Engineering Materials**

Johan Jansson

Doctoral Thesis in Materials and Manufacturing

Multiscale Constitutive Modeling of Heterogeneous Engineering Materials  
Dissertation Series No. 065

© 2021 Johan Jansson

Published by  
School of Engineering, Jönköping University  
P.O. Box 1026  
SE-551 11 Jönköping  
Tel. +46 36 10 10 00  
[www.ju.se](http://www.ju.se)

Printed by Stema Specialtryck AB, year 2021

ISBN 978-91-87289-69-9



# Acknowledgments

The work presented in this thesis was carried out during the years 2017 - 2021 at the department of Materials and Manufacturing at the School of Engineering, Jönköping University. I would like to thank my supervisors Associate Professor Kent Salomonsson and Associate Professor Jakob Olofsson for all of their support, discussions, knowledge, laughs and patience.

I would also like to thank my colleagues at the department of Materials and Manufacturing, as well as the department of Industrial Product Development, Production and Design for the laid back atmosphere and valuable discussions related to both material- and computational science.

Special thanks to Mirza Cenanovic, Carl-Johan Jonsson, and David Samvin for all of the memes, and for reminding me regularly to lock my office door, computers, and to encrypt all of my file systems and communications.

Lastly, and most importantly I want to thank Malin, Milo, Eddie and the rest of my family for all of their love and support.



Johan Jansson  
October, 2021





*With great processing power comes great responsibility*

- Hackerman





# Abstract

This work deals with different methods used to determine heterogeneous constitutive model parameters for macro-scale finite element models, based on microstructural variations, caused by the manufacturing process. These methods could be applied to decrease modeling errors associated with the material behavior, improving the predictive capabilities of structural analyses in simulation-driven industrial product development. By providing engineers with more sophisticated tools and methods which lets them consider the complex relationships between the manufacturing process, the resulting microstructure and the final properties, manufactured components have the potential to be further optimized with respect to both weight and performance, reducing their cost and environmental impact.

An empirical approach for cast components is presented in Papers I & II, where material testing is used as a basis for constitutive model parameter extraction via optimization. Linear models were created for both thermo-mechanical and thermo-physical material properties, by characterizing specimens extracted from different regions in a lamellar graphite cast iron cylinder head. These models were used to generate heterogeneous constitutive model parameters for the cylinder head, based on the solidification time as predicted by casting process simulations. The influence of several commonly made casting-specific engineering simplifications were investigated, and it was shown that non-trivial errors of a potentially large magnitude are introduced by not considering e.g. the compressive behavior of the material, residual stresses from the casting process, the temperature dependency of the material, or the process-induced heterogeneity.

Paper III describes a statistical homogenization-based method, for modeling of anisotropic fiber reinforced materials. A non-linear anisotropic constitutive model was developed and implemented in commercial finite element codes, which is able to consider heterogeneous fiber orientations using only one material definition. The anisotropic elastic constitutive tensor is determined from fiber-matrix homogenization, and orientation averaging using second- and fourth order fiber orientation tensors provided by injection molding simulations. The plastic constitutive parameters are determined by optimization

## *Abstract*

against experimental tensile tests using specimens with different fiber orientations. The method was demonstrated using a injection molded 50 wt.% short glass fiber reinforced plastic.

A pixel/voxel-based method is presented in Papers IV (2D) & V (3D), for simple and efficient generation of reduced numerical microstructure models using imaging data as input. The input micrograph or image stack is split into subdomains, which are evaluated individually using numerical or semi-analytical homogenization. The constitutive tensor of each subdomain is mapped to a new, reduced numerical model. The purpose of this approach was to support component level analyses, by representing process-induced microstructural imperfections like e.g. porosity on the macro-scale, in a computationally efficient way. The geometrical description of the microstructure can be retrieved from experimental imaging methods like Scanning Electron Microscopy (SEM) or X-ray based Computed Tomography (CT). Alternatively, it can be approximated from phase field or manufacturing process simulations. The method was demonstrated by reducing a 2D aluminium micrograph by 99.89%, with material property errors of less than 0.5% in Paper IV. Also, in paper V by reducing a complex high-resolution 3D aluminum shrinkage porosity by 99.2%, with a material property error of approximately 1%. The method significantly reduces the complexity of building finite element models of complex microstructures, where the pre-processing step is replaced by image segmentation.

# Thesis

This thesis provides an overview and summary of the following papers:

**Paper I:** *On the use of heterogeneous thermomechanical and thermophysical material properties in finite element analyses of cast components* by J. Jansson, J. Olofsson and K. Salomonsson.

Presented at the 5<sup>th</sup> International Symposium on Cutting Edge of Computer Simulation, of Solidification, Casting and Refining (ICASP-5 & CSSCR-5) June 2019 in Salzburg, Austria.

Author contributions: Carried out the numerical simulations. Analysed the results. Wrote the paper. Presented the paper at the conference.

**Paper II:** *Simulation-driven product development of cast components with allowance for process-induced material behaviour* by J. Jansson, J. Olofsson and K. Salomonsson.

Published in Journal of Computational Design and Engineering, March 2020.

Author contributions: Carried out the numerical simulations. Analysed the results. Wrote the paper.

**Paper III:** *An anisotropic non-linear material model for glass fibre reinforced plastics* by J. Jansson, T. Gustafsson, K. Salomonsson, J. Olofsson, J. Johansson, P. Appelsved and M. Palm.

Published in Composite Structures, April 2018.

Author contributions: Took part in planning the paper. Took part in developing the numerical method. Implemented the numerical method. Carried out the numerical simulations. Wrote the paper.

**Paper IV:** *Image-based semi-multiscale finite element analysis using elastic subdomain homogenization* by J. Jansson, K. Salomonsson and J. Olofsson.

Published in Meccanica, May 2021.

Author contributions: Took part in planning the paper. Took part in develop-

ing the numerical method. Implemented the numerical method. Carried out the numerical simulations. Wrote the paper.

**Paper V:** *Voxel-based semi-multiscale finite element analysis using elastic subdomain homogenization* by J. Jansson, K. Salomonsson and J. Olofsson.

Submitted manuscript.

Author contributions: Planned the paper. Developed the numerical method. Implemented the numerical method. Carried out the numerical simulations. Wrote the paper.

# Contents

<b>Acknowledgments</b>	<b>i</b>
<b>Abstract</b>	<b>v</b>
<b>Thesis</b>	<b>vii</b>
<b>1 Introduction</b>	<b>1</b>
1.1 Numerical modeling and simulations . . . . .	1
1.2 Simulation-driven product development . . . . .	3
1.3 Problem formulation . . . . .	5
<b>2 Microstructure of engineering materials</b>	<b>7</b>
2.1 Cast flake graphite iron (Papers I & II) . . . . .	7
2.2 Injection molded short GFRPs (Paper III) . . . . .	9
2.3 Cast aluminum (Papers IV & V) . . . . .	10
<b>3 Modeling of heterogeneous materials</b>	<b>13</b>
3.1 Elasticity . . . . .	14
3.2 Plasticity . . . . .	15
3.3 Homogenization . . . . .	17
3.4 Orientation averaging . . . . .	20
<b>4 Methodology</b>	<b>23</b>
4.1 Empirical method (Papers I & II) . . . . .	23
4.2 Statistical method (Paper III) . . . . .	24
4.3 Numerical/analytical method (Papers IV & V) . . . . .	26
<b>5 Conclusions</b>	<b>29</b>
5.1 Empirical method, cast flake graphite iron (Papers I & II) . . . .	29
5.2 Statistical method, injection molded short GFRPs (Paper III) .	31
5.3 Numerical/analytical method, cast aluminum (Papers IV & V)	33
<b>6 Future work</b>	<b>37</b>
<b>Bibliography</b>	<b>45</b>

## *Contents*

<b>Paper I</b>	<b>47</b>
<b>Paper II</b>	<b>57</b>
<b>Paper III</b>	<b>67</b>
<b>Paper IV</b>	<b>75</b>
<b>Paper V</b>	<b>91</b>

# Chapter 1

## Introduction

Research within the field of computational science is associated with the development, implementation and analysis of models and simulations, with the aim of understanding and solving complex problems. A *model* is an idealized mathematical description of the real-world behavior of some system, while a *simulation* refers to the process of evaluating such models using a set of input parameters. Simulations can be used together with experimental findings for verification or exploration, but also to investigate situations which would be impossible to evaluate experimentally due to technological or economical reasons. The possibilities provided by this fairly young field of research has led to it being considered as a potential third mode of science, together with experimental observation and theory [1]. In practice, the multidisciplinary nature of computational science leads to the development of *methods*, which have the potential of being applicable to both academic and industrial problems.

### 1.1 Numerical modeling and simulations

When attempting to model physical phenomena using numerical methods, errors are introduced in each activity that need to be understood and managed to produce high quality results. This becomes increasingly important if multiple simulations are connected, e.g. structural simulations using results from simulations of an initial manufacturing process. With the real-world behavior of the system under study as a point of reference, the error  $\Delta$  given by Eq. (1.1) is the sum of several accumulated errors, visible in the end as the difference between simulation results and reality. The following text briefly discusses some of these errors, which are also illustrated in Fig. 1.1, highlighting why a perfect match between simulations and experiments should not necessarily be expected.

$$\Delta = \Delta_{\text{modeling}} + \Delta_{\text{discretization}} + \Delta_{\text{solution}} + \Delta_{\text{validation}} \quad (1.1)$$

A mathematical description of any complex natural system starts with the act

of building an idealized model based on the observed physical phenomenon. Such models are built using physical laws, empirical relationships or fitting parameters without physical meaning [2]. Based on the simplifying assumptions and what phenomena the model aims to capture, its structure, complexity and applicability changes. The difference between the mathematical model and reality caused by this idealization process is the *modeling* error. For a structural finite element model, this error can be broken down further according to Eq. (1.2), highlighting commonly made simplifications to the geometry, load-case and how the material behaves.

$$\Delta_{\text{modeling}} = \Delta_{\text{geometry}} + \Delta_{\text{load-case}} + \Delta_{\text{material}} + \dots \quad (1.2)$$

Since we can not claim to fully understand nature, "*All models are wrong, but some are useful*" [3]. However, we can still strive towards minimizing the modeling error by including more aspects of the physical world as our knowledge and understanding increases.

The idealized mathematical models we come up with for physical systems typically consist of continuous Partial Differential Equations (PDE). Numerical methods like the Finite Element Method (FEM) or the Finite Volume Method (FVM) can be used to approximate the solution of these, given that the problem is properly discretized in space and time. The accuracy of the numerical model and the processing power required to solve it are conflicting objectives in this process. The difference between the continuous mathematical model and the discretized numerical model is the discretization error, where the influence of the discretization process can be quantified by e.g. performing sensitivity studies.

Since computers perform calculations using fixed-point arithmetic, truncation errors will accumulate during the solution process due to the large number of iterations sometimes required to solve the system of equations, i.e. a solution error will be introduced. If the applied numerical methods are implemented according to best practices, these errors are typically of lower significance.

The American Society of Mechanical Engineers (ASME) Guide for Verification and Validation in Computational Solid Mechanics [4] contains the following definitions:

*Verification is the process of determining that a computational model accurately represents the underlying mathematical model and its solution.*

*Validation is the process of determining the degree to which a model is an accurate representation of the real world from the perspective of the intended uses of the model.*

Two types of verification can be identified from this; code verification which refers to the act of establishing confidence in that the mathematical model



and solution algorithms are implemented correctly, and solution verification which refers to the act of establishing confidence in the discrete solution i.e. minimizing the discretization error. Under simple conditions, code verification can be achieved by comparing the model output with analytical or other known solutions. For more complicated problems, manufactured solutions might be applicable where the solution to a PDE is fabricated and substituted back into the PDE together with fitting boundary and initial conditions. The result is a forcing function which can be used as input to the code which; if error free, will reproduce the manufactured solution.

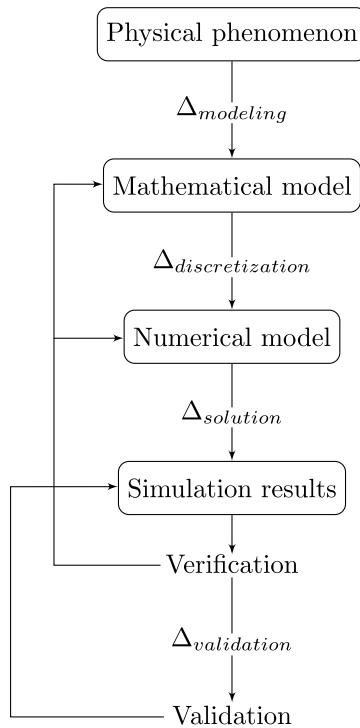


Figure 1.1: Important error sources in numerical modeling and simulations.

The aim of the validation process is to assess the predictive capability of the model by comparing simulation results to measurements from experiments. In the latter case, a validation (or measurement) error is introduced, since there are no perfect measurement devices.

## 1.2 Simulation-driven product development

Simulations are widely used in industrial product development, both to study the structural behavior of components under in-use conditions, but also to

study the manufacturing process. Structural simulations are applied in the early stages of product development e.g. as decision making support, or for idea generation, and in later stages to optimize performance, solve problems, verify requirements, or show compliance with laws and regulations. The Finite Element Method (FEM) is a numerical method used to solve PDEs, which is widely used in academic research, as well as in industrial product development. The act of applying the Finite Element Method in practice is commonly referred to as Finite Element Analysis (FEA), which includes the three practical steps of 1) building an idealized mathematical model, 2) performing simulations using the mathematical model, and 3) analyzing the simulation results. While the underlying method is the same, the conditions for successful application of FEA are different in academia and industry. Researchers typically have the privilege of a well-defined and fairly constant environment which in theory allows them to achieve a high degree of theoretical model accuracy, while the chaotic nature of real product development might force engineers to deal with key information that is missing, or changing rapidly with time. For reasons like these, as well as financial constraints, the requirements, complexity, and thus also the accuracy of the mathematical models tend to vary between these different environments. However, this does not stop consumer products from becoming more advanced with time, together with consistently increasing performance and sustainability requirements from both consumers and regulators. This creates a driving force towards more accurate, but simple and computationally efficient macro-scale methods for structural simulations, such that they are still applicable in industry.

Accurate finite element simulations rely on the use of constitutive models, which describe how the material behaves. These models are typically defined in terms of model parameters provided by some type of material testing. One common modeling error made in industrial product development is to treat the material of manufactured components as isotropic, homogeneous and free of imperfections. This effectively reduces the number of required experiments for determination of the constitutive model parameters, as well as the complexity of the numerical models. Some factor of ignorance is typically introduced to compensate for this assumption. However, in reality very few components are homogeneous, or free of imperfections after the manufacturing process. Depending on flow characteristics or other variations in processing conditions such as temperature distribution and cooling rate, the composition, morphology and quality of the resulting microstructure will vary locally as a function of component- and mold geometry. These microstructural variations lead to a heterogeneous distribution of material properties such as e.g. stiffness, hardening behavior, fatigue strength, physical properties and, thus, anisotropic constitutive behavior. For example, fatigue loaded cast components are especially sensitive to the influence of local imperfections such as porosity, oxides, pre-existing cracks or brittle inclusions [5, 6], most of which are not considered at all when using traditional constitutive modeling strategies.

### 1.3 Problem formulation

The *premise* of this work is that the macroscopic behavior of materials is a function of the underlying microstructure, and that the microstructure is a function of the processing conditions.

The *working hypothesis* has been that the complex relationships between process, microstructure and material properties need to be considered in simulation-driven product development. By decreasing the material modeling error in this context, more informed design decisions can be made, further optimizing performance metrics such as weight, cost and the environmental impact of industrially manufactured components.

The *purpose* and *aim* of this work has therefore been to develop and evaluate methods for the determination of heterogeneous constitutive model parameters, so that their influence on component performance can be better understood. This endeavor has been focused on simple macro-scale methods for finite element analyses of structural components, such that these methods can be considered and applied by industry in the early stages of simulation-driven product development.

More specifically, the following *objectives* were pursued:

- Evaluate the influence of material modeling errors for sand cast lamellar graphite iron components, such as the neglect of:
  - Heterogeneous material behavior
  - Residual stresses
  - Difference between tensile and compressive behavior
  - Temperature dependency
- Develop a method for the consideration of the heterogeneous fiber orientation in structural analyses of injection molded short glass fiber reinforced composites
- Develop and evaluate a method for the generation of reduced numerical microstructure models, based on 2D micrographs or 3D image stacks



## Chapter 2

# Microstructure of engineering materials

Selected aspects of the relationships between the manufacturing process, the complexity of the produced microstructure, and the resulting *heterogeneous* material properties are introduced and emphasized in this chapter. The discussion is limited to the materials and manufacturing processes considered in the appended papers, i.e. sand cast flake graphite iron, injection molded short fiber reinforced plastics and cast aluminum.

### 2.1 Cast flake graphite iron (Papers I & II)

Cast irons are among the most common, but also the most complex alloys used by industry. These materials are named based on the characteristic shape of the graphite phase, as illustrated by the numerical models in Fig. 2.1.

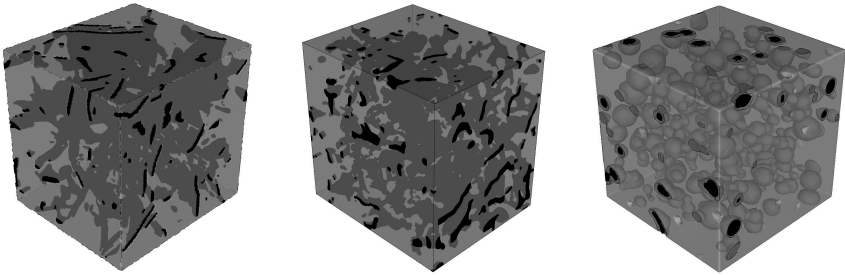


Figure 2.1: Numerical models of some characteristic cast iron alloy microstructures, reconstructed from X-ray based Computed Tomography (CT). In order of appearance from the left: Flake Graphite Iron (FGI), Compacted Graphite Iron (CGI) and Spherical Graphite Iron (SGI). Austenite and Ferrite in gray. Graphite in black. Model data from [7].

Flake Graphite Iron (FGI) is the most commonly used type of cast iron, and contains 2.5 - 4.0 wt.% Carbon (C), 1.0 - 3.0 wt.% Silicon (Si), and lower amounts of other alloying elements such as Phosphorous (P), Sulfur (S) and Manganese (Mn). The silicon promotes graphite growth, and suppresses the formation of iron carbides, while phosphorous improves fluidity. [8]

The solidification process of hypo-eutectic flake graphite iron starts with the formation of austenite dendrites. The size and shape of these dendrites are governed by the chemical composition of the melt, the cooling rate, as well as the inoculation conditions [9]. Carbon is rejected into the liquid until it reaches the eutectic composition of 4.3 wt.%, where both graphite and austenite are formed in a eutectic reaction. Furthermore, the morphology of the graphite, and the size of these eutectic cells are determined by the chemical composition, as well as the cooling- and inoculation conditions [10, 11, 12]. The resulting graphite morphology has been shown to influence both the elastic [13] and plastic [14] constitutive behavior of cast irons. A stronger material is obtained in general, by a more rapid solidification process, where the resulting structure, i.e. the graphite structure, the eutectic cells [12, 15], the dendritic network [16] and the pearlite lamellar spacing [17] becomes more refined.

Both elastic and plastic tensile and compressive properties have been shown to vary with temperature in cast irons [18]. Furthermore, the constitutive behavior differs significantly between tensile and compressive loading [19]. See e.g. Fig. 2.2a. This type of behavior is also seen in many other engineering materials, such as e.g. aluminum [20], concrete [21], and magnesium [22]. Holmgren, Dioszegi, and Svensson investigated heterogeneous physical properties, and found linear relationships for thermal conductivity, in terms of both carbon content and cooling rate. [23] It was found in [24], that lower cooling rates promote straight, long graphite flakes which result in higher thermal conductivity, while higher cooling rates leads to an increased fraction of primary austenite, which decreases thermal conductivity. As an example, see Fig. 2.2b.

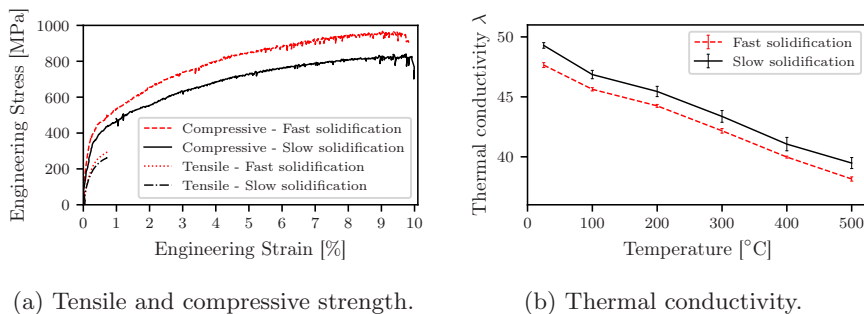


Figure 2.2: Mechanical and physical material properties as a function of solidification time for sand cast lamellar graphite iron. The difference between slow and fast solidification is approximately 1000 seconds. Results from [25].

## 2.2 Injection molded short GFRPs (Paper III)

Fiber Reinforced Plastics (FRP) are materials with discontinuous fibers embedded in a polymer matrix. These materials are widely used in automotive, naval and aerospace industries, due to their high specific strength and corrosion resistance. If properly utilized, such materials can be used to reduce the weight, cost and the environmental impact of load bearing components. Examples of polymer materials are polyester, vinyl ester or epoxy. Examples of fiber materials are glass, carbon, aramid and basalt, of up to 65 wt.%. For the case of short Glass Fiber Reinforced Plastics (GFRP), the fibers have a high stiffness with approximately linear mechanical response, as opposed to the non-linear polymer matrix in which they are dispersed. The combined effect of these constituents is a strongly anisotropic and non-linear composite material, also influenced by rate effects [26], temperature effects [27] and aging due to water absorption from the surrounding atmosphere [28]. While the injection molding process provides a large amount of design freedom, one issue is that the flow direction heavily influences the local fiber orientation. The fiber orientation is also influenced by factors such as the section thickness and the velocity profile. Near mold walls, fibers tend to align in parallel with the flow, while they align cross-flow in the center, and randomly in between [29, 30]. See Fig. 2.3a, which illustrates a typical, but simplified fiber orientation profile inside a injection molded plate. During manufacturing, the high pressure forces the fibers through the runner- and gating systems, which potentially leads to fiber- damage and length reduction [31]. The practical implications of this is that the in-use behavior of manufactured fiber reinforced components becomes hard to predict without using more sophisticated modeling strategies, which also consider the manufacturing process.

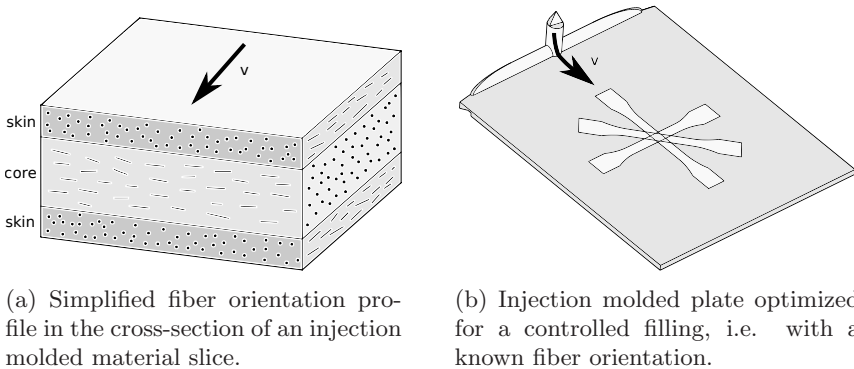


Figure 2.3: Fiber orientation due to flow in the  $v$  direction.

Several studies have been performed on the mechanical properties of these materials, focusing on the combined effect of fibers dispersed in a polymer

matrix [32, 33, 34, 29]. A commonly applied testing procedure is to produce specimens with a known, but varying fiber orientation relative to the intended loading direction. See e.g. the plate geometry in Fig. 2.3b, which is designed to induce a directional flow through the center of the plate. Such methods are sometimes denoted "off-axis" tests, and have been used extensively to show a strong non-linear relationship between both elastic and plastic constitutive behavior and the fiber orientation. Fig. 2.4 illustrates this for two composite materials, reinforced with different amounts of short glass fibers.

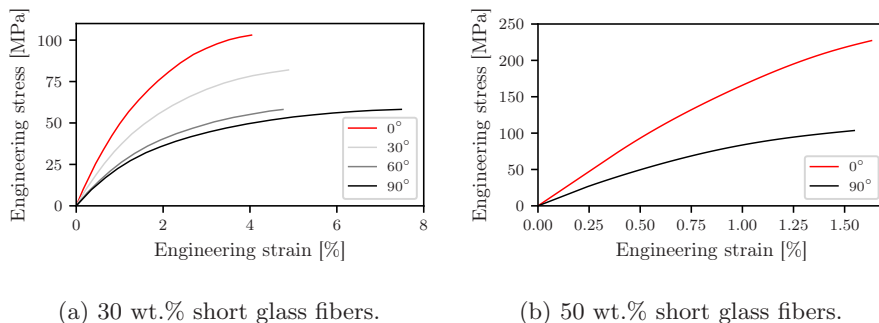


Figure 2.4: Mechanical behavior of two fiber reinforced plastics, evaluated using tensile testing at varying angles relative to the flow direction during injection molding. Results from [35].

## 2.3 Cast aluminum (Papers IV & V)

Mass production of cast aluminum components is made primarily using die casting, permanent mold casting, or sand casting. For die casting, a commonly used alloy is Al9Si3Cu(Fe), which contains approximately 9 wt.% Silicon (Si) for increased fluidity, 3 wt.% Copper (Cu) for precipitation hardening, and smaller amounts of Iron (Fe) for decreased mold erosion. During the solidification of such aluminum alloys, a primary dendritic phase grows. The rate at which the material solidifies strongly controls the coarseness of this dendritic structure. In thicker sections, where there is more time available for the solidification process, the distance between dendrite arms tends to be larger, while in thinner sections where solidification occurs more rapidly, it tends to be smaller [36]. Secondary alloying elements like silicon, copper and iron segregates between the primary dendrite arms, due to a decrease in solubility as the temperature decreases. The size, quantity and shape varies as a function of chemistry, cooling rate and the characteristics of the primary dendritic structure [37]. Strontium modification is commonly used to alter the morphology of silicon inclusions from larger plate-like, into smaller and rounder fibers, while heat treatment decreases inclusion connectivity and increases sphericity [37, 38, 39]. Other microstructural features of importance are shrinkage-



and gas porosities, as well as intermetallic phases. Since aluminum is cast at high temperatures, a large amount of liquid- and solid contraction occurs. The implications of this is that thinner regions, which solidify quickly, will block off feeding of still liquid metal to other, thicker regions, resulting in the formation of shrinkage pores as the material solidifies. Fig. 2.5 illustrates a voxel-reconstruction of an isolated shrinkage pore, which has most likely inherited its complex shape from the contraction of liquid nearby already solidified dendrites.

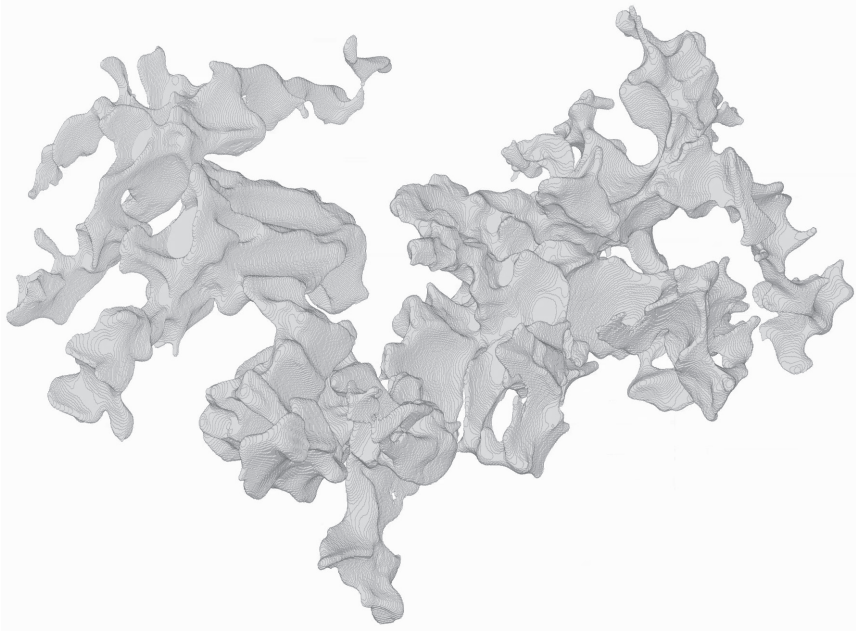


Figure 2.5: Cast aluminum alloy shrinkage porosity reconstructed from X-ray based Computed Tomography (CT).

Porosity also occurs in these alloys because of air which has been entrapped during the filling process, as well as due to hydrogen diffusion between the surrounding atmosphere and the metal, together with a decrease of hydrogen solubility during solidification [40]. Both porosity [41, 42, 43] and intermetallic phases [44, 45, 46, 47] tend to be complex interconnected 3D-structures [38, 48] whose size, distribution and morphology depends on chemistry, heat treatment and processing conditions such as the local cooling rate, or flow characteristics.

This highly complex three-dimensional, and heterogeneous structure controls the mechanical behavior of cast aluminum alloys [37]. The general coarseness of the microstructure has an influence on both yield strength, ultimate tensile strength and ductility, and is commonly described using the Secondary Den-

drite Arm Spacing (SDAS) [49]. The size and morphology of eutectic silicon which segregates between the primary dendrite arms during solidification has been shown to affect both ductility and strain hardening rate [50], and contributes to damage in the material during deformation via cracking parallel to the loading direction [51], or by debonding from the aluminum-silicon interface [52]. Iron-rich intermetallic compounds such as  $\beta$ -Fe have been proposed to act as stress concentrators, reducing ductility [5]. Damage contributions from intermetallic phases are due to debonding from the aluminum matrix, or by propagation of built-in cracks from nucleation on bifilms [53]. Oxides such as  $\text{Al}_2\text{O}_3$  form easily on the melt surface, and can be dragged into the casting during filling if the flow is violent enough. As these oxide films are solid and fold over themselves, they act as potential cracks in the material [54], but debonding at the oxide-matrix interface has also been observed [55]. Porosity leads to local stress concentration [56], and is the most common reason for fatigue crack initiation in cast aluminum components. [57] Other solid imperfections in the regions surrounding the pores are damaged further by the local concentration of stress during deformation. [58, 59] Porosity, as well as other imperfections have been shown to influence Low Cycle Fatigue (LCF,  $N < 10^5$ ) crack growth [59], as well as High Cycle Fatigue (HCF) damage [57]. For HCF, failure is primarily associated with persistent slip bands [60], however imperfections have also been observed to interact with the crack growth process [61]. The relative importance of the above mentioned microstructural imperfections has been studied by Wang et al. who showed that damage contribution from porosity and oxide films dominate when present, and can reduce fatigue life by one order of magnitude [5, 6].

The practical implications of the above discussion on cast materials is that for an increase in section thickness, the solidification time typically goes up, which results in a coarser microstructure and a higher risk of shrinkage porosity. The coarse microstructure is weaker on average, when compared to the finer structure achieved in thinner sections. Thus, the relationship between material strength and load bearing volume is non-intuitive for cast aluminum components, and needs to be considered by design engineers to produce high performing components.

## Chapter 3

# Modeling of heterogeneous materials

In the context of this thesis, the term *multiscale* refers to uncoupled consideration of the material microstructure, on the macroscale, using various approaches. This is motivated primarily by high requirements on computational efficiency, due to the strong emphasis on industrial applicability. In the following, Einstein's summation convention is implied for repeated indices. Newton's notation is used for differentiation with respect to time, i.e.  $\dot{v} = \frac{\partial v}{\partial t}$ , and  $u_{i,j}$  refers to the partial derivative  $\frac{\partial u_i}{\partial u_j}$ . Bold letters indicate vectors, or tensors expressed on Voigt form, while regular letters represent tensors on index form, or scalars.

Any continuum,  $\Omega$ , which is in balance with respect to mass, momentum, and which obeys the first law of thermodynamics can be described by the following field equations, and field variables, given by the continuity equation (3.1), the momentum equation (3.2), stress symmetry (3.3) and the energy equation (3.4)

$$\dot{\rho} + \rho v_{i,i} = 0, \quad (3.1)$$

$$\rho \dot{v}_i = \sigma_{ij,i} + \rho f_i, \quad (3.2)$$

$$\sigma_{ij} = \sigma_{ji}, \quad (3.3)$$

$$\rho \dot{e} = \sigma_{ij} v_{i,j} - q_{i,i} + \rho \epsilon. \quad (3.4)$$

Here,  $\rho$  is density,  $v_i$  is velocity,  $\sigma_{ij}$  is stress,  $f_i$  is volume force,  $e$  is internal energy,  $q_i$  is heat flux, and  $\epsilon$  is an internal heat source. A constitutive model is complementary to this system of equations and provides the missing unknowns by stating the relationship between stress  $\sigma_{ij}$  and strain  $\varepsilon_{ij}$ .

For *heterogeneous* materials, the constitutive behavior varies spatially throughout the continuum  $\Omega$ , as a function of the underlying microstructure for each

material point  $n$ . This could also be thought of as subdomains  $\Omega_n$ , as illustrated in Fig. 3.1.

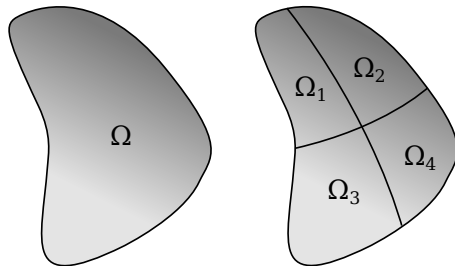


Figure 3.1: Heterogeneous continuum  $\Omega$ , with subdomains  $\Omega_1$ ,  $\Omega_2$ ,  $\Omega_3$  and  $\Omega_4$ .

### 3.1 Elasticity

In the case of anisotropic elasticity, we can use that  $\sigma_{ij}$  and  $\varepsilon_{kl}$  are symmetric second order tensors, which leads to minor symmetry of the fourth order constitutive tensor  $\mathcal{C}_{ijkl} = \mathcal{C}_{jikl} = \mathcal{C}_{ijlk} = \mathcal{C}_{jilk}$ . This allows us to formulate Hooke's generalized law of elasticity

$$\sigma_{ij} = \mathcal{C}_{ijkl} : \varepsilon_{kl} \quad (3.5)$$

on Voigt form, with  $\gamma_{ij} = 2\varepsilon_{ij}$  for  $i \neq j$

$$\begin{pmatrix} \sigma_{11} \\ \sigma_{22} \\ \sigma_{33} \\ \sigma_{23} \\ \sigma_{13} \\ \sigma_{12} \end{pmatrix} = \begin{pmatrix} \mathcal{C}_{1111} & \mathcal{C}_{1122} & \mathcal{C}_{1133} & \mathcal{C}_{1123} & \mathcal{C}_{1113} & \mathcal{C}_{1112} \\ \mathcal{C}_{2211} & \mathcal{C}_{2222} & \mathcal{C}_{2233} & \mathcal{C}_{2223} & \mathcal{C}_{2213} & \mathcal{C}_{2212} \\ \mathcal{C}_{3311} & \mathcal{C}_{3322} & \mathcal{C}_{3333} & \mathcal{C}_{3323} & \mathcal{C}_{3313} & \mathcal{C}_{3312} \\ \mathcal{C}_{2311} & \mathcal{C}_{2322} & \mathcal{C}_{2333} & \mathcal{C}_{2323} & \mathcal{C}_{2313} & \mathcal{C}_{2312} \\ \mathcal{C}_{1311} & \mathcal{C}_{1322} & \mathcal{C}_{1333} & \mathcal{C}_{1323} & \mathcal{C}_{1313} & \mathcal{C}_{1312} \\ \mathcal{C}_{1211} & \mathcal{C}_{1222} & \mathcal{C}_{1233} & \mathcal{C}_{1223} & \mathcal{C}_{1213} & \mathcal{C}_{1212} \end{pmatrix} \begin{pmatrix} \varepsilon_{11} \\ \varepsilon_{22} \\ \varepsilon_{33} \\ \gamma_{23} \\ \gamma_{13} \\ \gamma_{12} \end{pmatrix}. \quad (3.6)$$

For a heterogeneous material, the elastic constitutive tensor  $\mathcal{C}_{ijkl}$  varies spatially for each subdomain  $\Omega_i$ . If we also assume small deformations, major symmetries of  $\mathcal{C}_{ijkl} = \mathcal{C}_{klij}$  apply, and we can write the above relation as

$$\begin{pmatrix} \sigma_1 \\ \sigma_2 \\ \sigma_3 \\ \sigma_4 \\ \sigma_5 \\ \sigma_6 \end{pmatrix} = \begin{pmatrix} C_{11} & C_{12} & C_{13} & C_{14} & C_{15} & C_{16} \\ & C_{22} & C_{23} & C_{24} & C_{25} & C_{26} \\ & & C_{33} & C_{34} & C_{35} & C_{36} \\ & & & C_{44} & C_{45} & C_{46} \\ & & & & C_{55} & C_{56} \\ & & & & & C_{66} \end{pmatrix} \begin{pmatrix} \varepsilon_1 \\ \varepsilon_2 \\ \varepsilon_3 \\ \varepsilon_4 \\ \varepsilon_5 \\ \varepsilon_6 \end{pmatrix}, \quad (3.7)$$

or more compactly  $\boldsymbol{\sigma} = \mathbf{C}\boldsymbol{\varepsilon}$ . For the specific case of orthotropy, this relationship can be expressed as

$$\begin{pmatrix} \sigma_1 \\ \sigma_2 \\ \sigma_3 \\ \sigma_4 \\ \sigma_5 \\ \sigma_6 \end{pmatrix} = \begin{pmatrix} \frac{1}{E_{11}} & -\frac{\nu_{21}}{E_{22}} & -\frac{\nu_{31}}{E_{33}} & 0 & 0 & 0 \\ -\frac{\nu_{12}}{E_{11}} & \frac{1}{E_{22}} & -\frac{\nu_{32}}{E_{33}} & 0 & 0 & 0 \\ -\frac{\nu_{13}}{E_{11}} & -\frac{\nu_{23}}{E_{22}} & \frac{1}{E_{33}} & 0 & 0 & 0 \\ 0 & 0 & 0 & \frac{1}{G_{23}} & 0 & 0 \\ 0 & 0 & 0 & 0 & \frac{1}{G_{13}} & 0 \\ 0 & 0 & 0 & 0 & 0 & \frac{1}{G_{12}} \end{pmatrix}^{-1} \begin{pmatrix} \varepsilon_1 \\ \varepsilon_2 \\ \varepsilon_3 \\ \varepsilon_4 \\ \varepsilon_5 \\ \varepsilon_6 \end{pmatrix}, \quad (3.8)$$

or more compactly  $\boldsymbol{\sigma} = \mathbf{K}^{-1}\boldsymbol{\varepsilon}$ , where  $\mathbf{K}$  is the compliance tensor.

Here,  $E_{ii}$  (without summation) is the stiffness along the  $i$ -axis,  $G_{ij}$  is the shear modulus in the  $j$ -direction, on the plane with normal  $i$  and  $\nu_{ij}$  is Poisson's ratio due to an extension along  $i$ , with a contraction along  $j$ . For transversely isotropic materials, such as a composite material with circular fibers aligned along the 1-axis,  $E_{22} = E_{33}$  and  $G_{12} = G_{13}$  as well as  $\nu_{12} = \nu_{13}$  and so on. For the special case of isotropic elasticity, all components  $E_{ii}$  (no summation),  $G_{ij}$  and  $\nu_{ij}$  are the same.

## 3.2 Plasticity

The classical continuum approach for plasticity is to introduce a yield criterion, which is used to determine when the material starts to deform irreversibly, e.g. via dislocation motion for metallic materials. First, the stress tensor  $\sigma_{ij}$ , can be additively decomposed into volumetric and deviatoric components

$$\sigma_{ij} = \sigma^v \delta_{ij} + \sigma_{ij}^d, \quad (3.9)$$

where the volumetric part  $\sigma^v$  is the scalar average of the normal stress components, associated with volume change

$$\sigma^v = \frac{1}{3}(\sigma_{11} + \sigma_{22} + \sigma_{33}), \quad (3.10)$$

and the deviatoric part  $\sigma_{ij}^d$  is what is left after subtracting the volumetric part, i.e. associated with shear stress and shape change

$$\sigma_{ij}^d = \sigma_{ij} - \sigma^v \delta_{ij}. \quad (3.11)$$

Here,  $\delta_{ij}$  is the Kronecker delta defined as

$$\delta_{ij} = \begin{cases} 0 & \text{for } i \neq j, \\ 1 & \text{for } i = j. \end{cases} \quad (3.12)$$

For ductile metals, the von Mises yield criterion is commonly used, based on the assumption that only deviatoric stress contributes to plastic deformation.

This can be formulated as the inequality

$$\sqrt{\frac{3}{2} \sigma_{ij}^d : \sigma_{ij}^d} \leq \sigma^y, \quad (3.13)$$

i.e. the stress state is elastic when the effective von Mises stress is lower than the uni-axial yield strength  $\sigma^y$ . This can be stated as a yield function

$$\theta = |\sigma^y| - \sqrt{\frac{3}{2} \sigma_{ij}^d : \sigma_{ij}^d}, \quad (3.14)$$

for which  $\theta = 0$  defines a yield surface in stress-space. In the above case, this surface takes the form of a hyper-cylinder, or a regular cylinder of radius  $r = \sigma_y \sqrt{2/3}$  in principal stress space. For any given stress-state where the yield condition is not met, elasticity applies. For all other cases, plastic deformation occurs. In plasticity delimited to small deformations, it is assumed that the total strain can be additively decomposed into elastic and plastic strain components

$$\varepsilon_{ij} = \varepsilon_{ij}^e + \varepsilon_{ij}^p. \quad (3.15)$$

In the case of metal plasticity, the plastic strain  $\varepsilon_{ij}^p$  is commonly given by an associative flow rule on rate form as

$$\dot{\varepsilon}_{ij}^p = \mu \frac{\partial \theta}{\partial \sigma_{ij}}, \quad (3.16)$$

in terms of a plastic multiplier  $\mu$ , with the conditions  $\mu \geq 0$ ,  $\theta \leq 0$  and  $\mu \theta = 0$ . These conditions enforce the dissipation inequality  $D \geq 0$ , i.e. the energy release associated with plastic deformation cannot return back into the system. A characteristic uni-axial material response which highlights this is given in Fig. 3.2, where  $\Psi$  is the total strain energy.

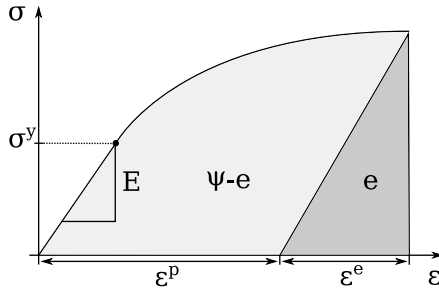


Figure 3.2: Uni-axial material response, with elastic stiffness  $E$ , initial yield point  $\sigma^y$ . The strain energy  $e$ , associated with elastic strain  $\varepsilon^e$ , remains in the material after unloading, while the strain energy  $\Psi - e$ , associated with plastic strain  $\varepsilon^p$ , dissipates.

Lastly, a hardening rule describes how the yield-surface evolves with plastic strain. Geometrically, this is represented by expansion, and/or translation of

the yield surface in principal stress space. For a heterogeneous material, the hardening rule can e.g. be given locally by a function on the form  $\kappa(\boldsymbol{\varepsilon}^p, \mathbf{x}_n)$ , where the vector  $\mathbf{x}_n$  varies with the subdomain  $\Omega_n$ , and contains the microstructure related variables influencing the flow stress of the material.

### 3.3 Homogenization

Instead of performing macro-scale experimental material testing to determine constitutive model parameters, homogenization methods lets us calculate effective properties, based on information regarding the micro-scale constituents. The volume averaged quantity  $\hat{\bullet}$  in the domain  $\Omega$ , with volume  $V$ , is defined as

$$\hat{\bullet} = \frac{1}{V} \int_{\Omega} \bullet \, d\Omega. \quad (3.17)$$

Here,  $\bullet$  can be any local quantity, indicated by a subscript star in the following, such as e.g. stress  $\boldsymbol{\sigma}_*$ , strain  $\boldsymbol{\varepsilon}_*$  or the constitutive tensor  $\mathbf{C}_*$ . By applying Eq. (3.17) to a subdomain  $\Omega_n$ , the upper bound of the effective elastic properties  $\hat{\mathbf{C}}_n^V$  can be retrieved by making the Voigt assumption of a constant micro-scale strain field, i.e.  $\boldsymbol{\varepsilon}_n = \hat{\boldsymbol{\varepsilon}}_n$  in  $\Omega_n$ , which leads to

$$\hat{\mathbf{C}}_n^V = \frac{1}{V} \int_{\Omega_n} \mathbf{C}_* \, d\Omega_n, \quad (3.18)$$

whereas the lower bound of the effective elastic properties  $\hat{\mathbf{C}}_n^R$  can be retrieved by making the Reuss assumption of a constant micro-scale stress field i.e.  $\boldsymbol{\sigma}_n = \hat{\boldsymbol{\sigma}}_n$  in  $\Omega_n$ , which leads to

$$\hat{\mathbf{C}}_n^R = \left( \frac{1}{V} \int_{\Omega_n} \mathbf{C}_*^{-1} \, d\Omega_n \right)^{-1}. \quad (3.19)$$

The Reuss and Voigt bounds are the most extreme that can be put on the true elastic constitutive tensor  $\mathbf{C}_n$  of  $\Omega_n$ , i.e.

$$\hat{\mathbf{C}}_n^R \leq \mathbf{C}_n \leq \hat{\mathbf{C}}_n^V. \quad (3.20)$$

The Reuss-Voigt-Hill average [62] of these bounds is commonly used as an approximation for the constitutive tensor

$$\bar{\mathbf{C}}_n^{RV} = \frac{\hat{\mathbf{C}}_n^R + \hat{\mathbf{C}}_n^V}{2}. \quad (3.21)$$

Even narrower lower,  $\mathbf{C}_n^L$  and upper  $\mathbf{C}_n^U$ , bounds were defined by Hashin and Shtrikman [63] by assuming isotropy for a two-phase material, i.e.

$$\hat{\mathbf{C}}_n^R \leq \mathbf{C}_n^L \leq \mathbf{C}_n \leq \mathbf{C}_n^U \leq \hat{\mathbf{C}}_n^V. \quad (3.22)$$

These bounds are given here in terms of the bulk  $K_p$  and shear modulus  $G_p$  for the phases  $p \in [1, 2]$  with volume fractions  $f_p$ ,

$$K_n^U = K_2 + \frac{f_1}{\frac{1}{K_1 - K_2} + \frac{3f_2}{3K_2 + 4G_2}}, \quad (3.23)$$

$$K_n^L = K_1 + \frac{f_2}{\frac{1}{K_2 - K_1} + \frac{3f_1}{3K_1 + 4G_1}}, \quad (3.24)$$

$$G_n^U = G_2 + \frac{f_1}{\frac{1}{G_1 - G_2} + \frac{6(K_2 + 2G_2)f_2}{5G_2(3K_2 + 4G_2)}}, \quad (3.25)$$

$$G_n^L = G_1 + \frac{f_2}{\frac{1}{G_2 - G_1} + \frac{6(K_1 + 2G_1)f_1}{5G_1(3K_1 + 4G_1)}}, \quad (3.26)$$

and  $K_2 > K_1$ ,  $G_2 > G_1$ . The averages  $\bar{K}_n$  and  $\bar{G}_n$

$$\bar{K}_n = \frac{K_n^U + K_n^L}{2}, \quad (3.27)$$

$$\bar{G}_n = \frac{G_n^U + G_n^L}{2}, \quad (3.28)$$

can then be used together with the well known relationships

$$\bar{E}_n = \frac{9\bar{K}_n\bar{G}_n}{3\bar{K}_n + \bar{G}_n}, \quad (3.29)$$

$$\bar{\nu}_n = \frac{3\bar{K}_n - 2\bar{G}_n}{2(3\bar{K}_n + \bar{G}_n)}, \quad (3.30)$$

$$\bar{K}_n = \frac{\bar{E}_n}{3(1 - 2\bar{\nu}_n)}, \quad (3.31)$$

$$\bar{G}_n = \frac{\bar{E}_n}{2(1 + \bar{\nu}_n)}, \quad (3.32)$$

to approximate the averaged constitutive tensor  $\bar{\mathbf{C}}_n^{HS}$ , i.e.  $\mathbf{C}_n^L \leq \bar{\mathbf{C}}_n^{HS} \leq \mathbf{C}_n^U$ .

The effective elastic tensor  $\bar{\mathbf{C}}_n$  of a composite material containing an inclusion/void, can be expressed in terms of the two phases  $p \in [1, 2]$ , with volume fractions  $f_p$  and constitutive tensors  $\mathbf{C}_p$ , following results from Eshelby [64], Benveniste [65], Mori, Tanaka [66] and Mura [67] as

$$\bar{\mathbf{C}}_n = \mathbf{C}_1 + f_2(\mathbf{C}_2 - \mathbf{C}_1)\mathbf{A}. \quad (3.33)$$

With the strain concentration tensor

$$\mathbf{A} = [\mathbf{I} + \mathbf{S}\mathbf{C}_1^{-1}(\mathbf{C}_2 - \mathbf{C}_1)]^{-1}[(1 - f_2)\mathbf{I} + f_2[\mathbf{I} + \mathbf{S}\mathbf{C}_1^{-1}(\mathbf{C}_2 - \mathbf{C}_1)]^{-1}]^{-1}. \quad (3.34)$$



Here,  $\mathbf{I}$  is the fourth order identity tensor written on Voigt form

$$\mathbf{I} = \begin{pmatrix} 1 & 0 & 0 & 0 & 0 & 0 \\ & 1 & 0 & 0 & 0 & 0 \\ & & 1 & 0 & 0 & 0 \\ & & & \frac{1}{2} & 0 & 0 \\ & & & & \frac{1}{2} & 0 \\ & & & & & \frac{1}{2} \end{pmatrix}, \quad (3.35)$$

and  $\mathbf{S}$  is Eshelby's tensor, which differs depending on the inclusion shape. For the case of a spherical inclusion, such as a spherical gas pore inside a metallic material with Poisson's ratio  $\nu$ ,

$$\mathbf{S}^s = \begin{pmatrix} \frac{7-5\nu}{15(1-\nu)} & \frac{5\nu-1}{15(1-\nu)} & \frac{5\nu-1}{15(1-\nu)} & 0 & 0 & 0 \\ \frac{5\nu-1}{15(1-\nu)} & \frac{7-5\nu}{15(1-\nu)} & \frac{5\nu-1}{15(1-\nu)} & 0 & 0 & 0 \\ \frac{5\nu-1}{15(1-\nu)} & \frac{5\nu-1}{15(1-\nu)} & \frac{7-5\nu}{15(1-\nu)} & 0 & 0 & 0 \\ 0 & 0 & 0 & \frac{2(4-5\nu)}{15(1-\nu)} & 0 & 0 \\ 0 & 0 & 0 & 0 & \frac{2(4-5\nu)}{15(1-\nu)} & 0 \\ 0 & 0 & 0 & 0 & 0 & \frac{2(4-5\nu)}{15(1-\nu)} \end{pmatrix}. \quad (3.36)$$

For the case of a cylindrical inclusion, such as a reinforcing fiber inside a polymer matrix with Poisson's ratio  $\nu$ ,

$$\mathbf{S}^c = \begin{pmatrix} 0 & 0 & 0 & 0 & 0 & 0 \\ \frac{\nu}{2(1-\nu)} & \frac{5-4\nu}{8(1-\nu)} & \frac{4\nu-1}{8(1-\nu)} & 0 & 0 & 0 \\ \frac{\nu}{2(1-\nu)} & \frac{4\nu-1}{8(1-\nu)} & \frac{5-4\nu}{8(1-\nu)} & 0 & 0 & 0 \\ 0 & 0 & 0 & \frac{1}{4} & 0 & 0 \\ 0 & 0 & 0 & 0 & \frac{3-4\nu}{8(1-\nu)} & 0 \\ 0 & 0 & 0 & 0 & 0 & \frac{1}{4} \end{pmatrix}. \quad (3.37)$$

Eshelby's tensor for other simple inclusion shapes are given in the book by Mura [67]. For the case of inclusion-inclusion interactions, for example when using large amounts of reinforcing fibers,  $\bar{\mathbf{C}}_n$  can be approximated by recursive substitution back into Eq. (3.33). [68]

For the case of arbitrary microstructural geometries, numerical homogenization methods are required. For a given strain field  $\varepsilon_{ij}$  applied to the computational cell  $\Omega_n$ , the elastic constitutive model parameters can be solved for by using Hooke's law, based on the resulting stress field  $\sigma_{ij}$ . To determine the nine engineering constants  $E_{ii}$  (without summation),  $\nu_{ij}$ ,  $G_{ij}$  from Eq. (3.8) for a known but arbitrary microstructure, six numerical models need to be built, solved and post-processed. This is illustrated for displacement controlled uni-axial loading in Fig. 3.3, and for shear loading in Fig. 3.4.

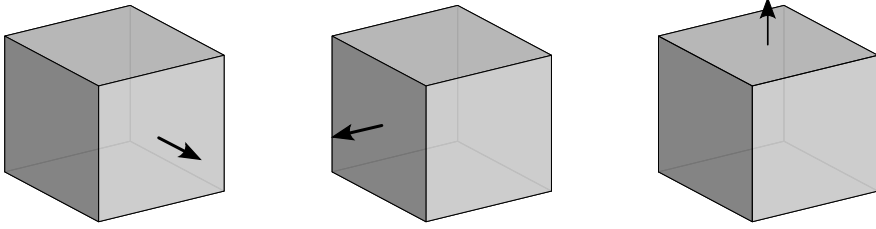


Figure 3.3: Loading conditions for the determination of  $E_{11}$ ,  $\nu_{12}$  and  $\nu_{13}$  (left),  $E_{22}$ ,  $\nu_{21}$  and  $\nu_{23}$  (middle) and  $E_{33}$ ,  $\nu_{31}$  and  $\nu_{32}$  (right).

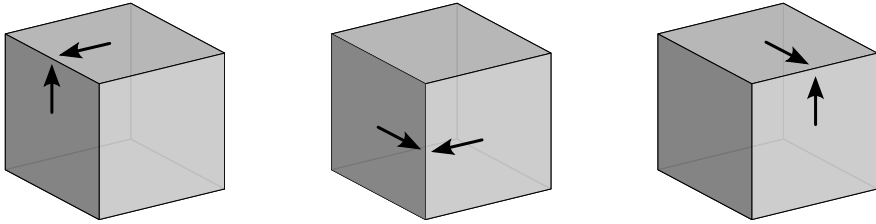


Figure 3.4: Loading conditions for the determination of  $G_{23}$  (left),  $G_{13}$  (middle) and  $G_{12}$  (right).

In practice, this involves computing the stress  $\sigma_{ij}$  from the nodal reaction forces  $\sum F$  for each side of the computational cell with area  $A$ , due to the strain  $\varepsilon_{ij}$  imposed by some displacement boundary condition. Nodal Periodic Boundary Conditions (PBC) can be applied to opposing faces as constraint equations, such that they are allowed to distort freely without remaining plane [69]. This implies that the overall material structure is periodic. The practical details are described in further detail in the Abaqus [70] EasyPBC plugin paper by Omairey et al. [71].

### 3.4 Orientation averaging

The probability of finding a fiber in any particular direction can be described by a probability distribution function  $\psi(\mathbf{p})$ , where

$$\mathbf{p} = \begin{pmatrix} \sin(\theta)\cos(\phi) \\ \sin(\theta)\sin(\phi) \\ \cos(\theta) \end{pmatrix}, \quad (3.38)$$

is the unit-vector spanning the unit-sphere with polar- and azimuthal angles  $\theta$  and  $\phi$ , as illustrated by Fig. 3.5.

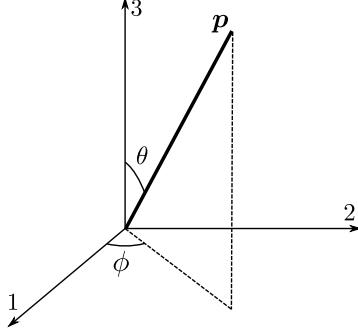


Figure 3.5: Fiber oriented along  $\pm \mathbf{p}$ , fully defined by the angles  $\theta \in [0, \pi]$  and  $\phi \in [0, 2\pi]$ .

Integrating the product between  $\mathbf{p}$  and the probability distribution function  $\psi(\mathbf{p})$  results in a symmetric second order fiber orientation tensor

$$\tau_{ij} = \int_0^{2\pi} \int_0^\pi p_i p_j \psi(\mathbf{p}) d\theta d\phi = \begin{bmatrix} \tau_{11} & \tau_{12} & \tau_{13} \\ & \tau_{22} & \tau_{23} \\ & & \tau_{33} \end{bmatrix}, \quad (3.39)$$

where the diagonal entries represent the likelihood of finding fibers along the 11-, 22- and 33-axis, i.e.  $\tau_{ii} = 1$ . A hybrid closure approximation can be used to obtain a fourth order orientation tensor based on the second order one

$$\mathcal{T}_{ijkl} = \left( \frac{3}{2} - \frac{3}{2} \tau_{mn} \tau_{mn} \right) \mathcal{T}_{ijkl}^\alpha + \mathcal{T}_{ijkl}^\beta, \quad (3.40)$$

$$\mathcal{T}_{ijkl}^\alpha = -\frac{1}{35} (\delta_{ij} \delta_{kl} + \delta_{ik} \delta_{jl} + \delta_{il} \delta_{jk}) + \frac{1}{7} (\tau_{ij} \delta_{kl} + \tau_{ik} \delta_{jl} + \tau_{il} \delta_{jk} + \tau_{kl} \delta_{ij} + \tau_{jl} \delta_{ik} + \tau_{jk} \delta_{il}), \quad (3.41)$$

$$\mathcal{T}_{ijkl}^\beta = \tau_{ij} \tau_{kl}. \quad (3.42)$$

The linear part  $\mathcal{T}_{ijkl}^\alpha$  provides an exact solution for random fiber orientations ( $\tau_{11} = \tau_{22} = \tau_{33} = 1/3$ ), while the non-linear part  $\mathcal{T}_{ijkl}^\beta$  provides an exact solution for a fully aligned fiber orientation ( $\tau_{11} = 1$ ,  $\tau_{22} = 1$ , or  $\tau_{33} = 1$ ). To proceed, the effective constitutive tensor  $\bar{\mathbf{C}}_n$ , for a cylindrical fiber embedded in a matrix material is needed, and can be computed based on Eq. (3.33). The orientation averaged fourth order stiffness tensor  $\bar{\mathcal{C}}_{ijkl}$  is then given in [72] by

$$\begin{aligned} \bar{\mathcal{C}}_{ijkl} = & B_1(\mathcal{T}_{ijkl}) + B_2(\tau_{ij} \delta_{kl} + \tau_{kl} \delta_{ij}) \\ & + B_3(\tau_{ik} \delta_{jl} + \tau_{il} \delta_{jk} + \tau_{jl} \delta_{ik} + \tau_{jk} \delta_{il}) \\ & + B_4(\delta_{ij} \delta_{kl}) + B_5(\delta_{ik} \delta_{jl} + \delta_{il} \delta_{jk}), \end{aligned} \quad (3.43)$$

where  $B_c$  refers to the entries of  $\bar{\mathbf{C}}_n$  according to Eq. (3.7), with

$$B_1 = \bar{C}_{11} + \bar{C}_{22} - 2\bar{C}_{12} - 4\bar{C}_{66}, \quad (3.44)$$

$$B_2 = \bar{C}_{12} - \bar{C}_{23}, \quad (3.45)$$

$$B_3 = \bar{C}_{66} + \frac{1}{2}\bar{C}_{23} - \frac{1}{2}\bar{C}_{22}, \quad (3.46)$$

$$B_4 = \bar{C}_{23}, \quad (3.47)$$

$$B_5 = \frac{1}{2}\bar{C}_{22} - \frac{1}{2}\bar{C}_{23}. \quad (3.48)$$

This operation represents a rotation of the homogenized fiber-matrix composite, initially oriented along the 1-axis, into the most likely direction based on the probabilities of the given fiber orientation tensor  $\tau_{ij}$ , as illustrated by Fig. 3.6.

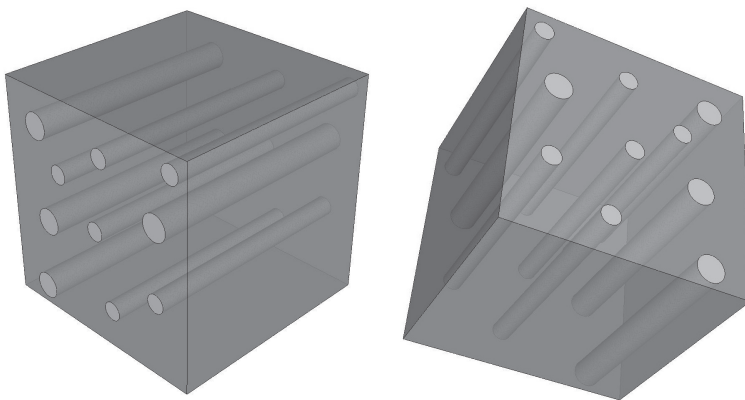


Figure 3.6: Orientation averaging based on the fiber orientation tensors  $\tau_{ij}$  and  $\mathcal{T}_{ijkl}$ . Left:  $\bar{\mathbf{C}}_n$  from homogenization by Eq. (3.33). Right: rotation of  $\bar{\mathbf{C}}_n$  into  $\bar{\mathbf{C}}_{ijkl}$  using Eq. (3.43).

# Chapter 4

## Methodology

This chapter summarizes the methodologies which were developed and applied in the appended papers, i.e. different strategies for the generation and application of heterogeneous constitutive model parameters, based on local microstructural variations, caused by the manufacturing process.

### 4.1 Empirical method (Papers I & II)

A simple one-dimensional empirical model, commonly used for cast metals which are approximately isotropic on the macro-scale, is given by  $\sigma = E\varepsilon_e$  when elastic, and  $\sigma = K\varepsilon_p^n$  when plastic. Here,  $E$  is the material stiffness,  $K$  is known as the strength coefficient and  $n$  the strain hardening coefficient. The constitutive model parameters  $E = E(\mathbf{x})$ ,  $K = K(\mathbf{x})$ , and  $n = n(\mathbf{x})$  are functions of the microstructure via the vector  $\mathbf{x}$  for the reasons discussed in Chapter 2. The vector  $\mathbf{x}$  could contain any microstructural or process-related measurable variables such as e.g. dendrite arm spacing, solidification time, etc. The classical approach of finding these constitutive parameters is to minimize the objective function which describes the difference between the constitutive model and experimental data from uni-axial, bi-axial or pure shear testing.

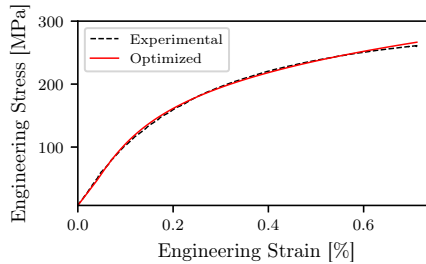


Figure 4.1: Constitutive model parameters extracted by optimization against an experimental stress-strain curve associated with a known solidification time.

Fig. 4.1 illustrates the result of this for a uni-axial tensile test performed at room temperature, with a specific sample solidification time, i.e. both temperature  $T$  and microstructural parameters  $\mathbf{x}$  are approximately fixed. The optimization process is then performed multiple times, for samples of different characteristic microstructure, by controlling the processing conditions using e.g. a Bridgman furnace with a fixed solidification time, or by extraction from specific regions in manufactured components. From multiple such measurements and optimizations, the constitutive model parameters can be expressed as functions of the local microstructure or processing conditions. These functions can then be used together with processing simulations, to generate heterogeneous and element specific constitutive model parameters.

In Papers I & II, this method was applied to a sand cast flake graphite iron cylinder head, with the purpose of investigating the influence of neglecting process-induced, temperature dependent and stress-state dependent mechanical and physical properties, as well as the influence of neglecting residual stresses from the casting process. Both structural and thermal simulations were performed in these studies, with varying levels of detail removed in the material data. The solidification time, as well as the residual stress state was predicted using an initial solidification simulation. The residual stress tensor components were mapped from the finite difference mesh to the corresponding element in the finite element mesh by using MAGMALink, where they were prescribed as initial conditions. A numerical reference model which contained all available material data was then used to assess the effects of the above mentioned modeling errors, by successive subtraction of the stress- and temperature fields.

## 4.2 Statistical method (Paper III)

To determine the elastic constitutive behavior of anisotropic fiber reinforced plastics, a combination of analytical and statistical approaches were used. The combined stiffness of a fiber reinforcement dispersed in a polymer matrix depends on the constitutive properties of both phases, as well as the shape of the reinforcement. The homogenized constitutive tensor  $\bar{\mathbf{C}}_n$  given by Eq. (3.33) was used, where  $\mathbf{C}_1$  represents the constitutive behavior of the matrix phase, and  $\mathbf{C}_2$  that of the fiber phase, with volume fraction  $v_2$ . Eshelby's tensor  $\mathbf{S}$  was approximated using the expression for cylindrical inclusions defined by Eq. (3.37), together with the identity tensor  $\mathbf{I}$  in Eq. (3.35) and the strain concentration tensor  $\mathbf{A}$  in Eq. (3.34). For fiber volume fractions above 30%, the homogenization was performed in two steps. First, the interaction between fiber and matrix is considered. Then, the pure matrix  $\mathbf{C}_1$  is replaced by the already homogenized composite  $\bar{\mathbf{C}}_n$ . In other words,  $\bar{\mathbf{C}}_n$  is inserted recursively into itself as the new reinforced matrix  $\bar{\mathbf{C}}_1$ . This should be interpreted as a consideration of fiber-fiber interaction, with the new calibration parameter  $\bar{v}_2$ . These operations result in a transversely isotropic stiffness ten-

sor, i.e. all fibers are aligned along one direction, e.g. the 1-direction which implies  $E_{11} > (E_{22} = E_{33})$ . The statistically orientation averaged constitutive tensor  $\bar{\mathbf{C}}_{ijkl}$  given by Eq. (3.43) can now be determined, which rotates the transversely isotropic stiffness tensor  $\bar{\mathbf{C}}_n$ , now expressed in terms of the coefficients  $B_c$  given by Eqs. 3.44 - 3.48, into the most likely direction of fibers by considering the fiber orientation tensors  $\tau_{ij}$  and  $\mathcal{T}_{ijkl}$  given by Eqs. (3.39) and (3.40). The non-linear constitutive behavior was then described using the following hardening functional

$$\kappa(\varepsilon_p, \tau_{ij}) = Y(\tau_{ij}) - \frac{H(\tau_{ij})}{A(\tau_{ij})}(e^{A(\tau_{ij})\varepsilon_p} - 1), \quad (4.1)$$

which depends on the effective plastic strain  $\varepsilon_p$  and the fiber orientation tensor  $\tau_{ij}$  via the non-linear hardening polynomials  $Y$ ,  $H$  and  $A$ . Here,  $Y$  represents the yield stress of the material, while  $A$  and  $H$  both control the characteristics of the non-linear response. As an example, for three off-axis tests, the function  $Y$  would take the following Lagrangian form

$$Y(x) = \frac{(x - x_2)(x - x_3)}{(x_1 - x_2)(x_1 - x_3)}y_1 + \frac{(x - x_1)(x - x_3)}{(x_2 - x_1)(x_2 - x_3)}y_2 + \frac{(x - x_1)(x - x_2)}{(x_3 - x_1)(x_3 - x_2)}y_3. \quad (4.2)$$

Here,  $x_n \in [0, 1]$  represents known diagonal entries of the second order fiber orientation tensor  $\tau_{ij}$ , with  $y_n$  being the corresponding values of  $Y$ . As an example, for the anisotropic tensile tests illustrated in Fig. 2.4b,  $Y \approx 25$  MPa for a  $90^\circ$  fiber orientation, and  $Y \approx 50$  MPa for a  $0^\circ$  fiber orientation, i.e.  $Y(x)$  is defined by the data points  $(x_1, y_1) = (0, 25)$  and  $(x_3, y_3) = (1, 50)$ . The values of  $y_n$  in  $Y$ ,  $H$  and  $A$  thus become material-specific, and are determined by simultaneous optimization towards multiple off-axis tests. These interpolating polynomials are then used to set the plastic material parameters.

In Paper III, the above method is demonstrated for a injection molded 50 wt.% glass fiber reinforced material, using the commercial finite element code LS-DYNA [73]. A custom material subroutine was developed to implement the elastic and plastic constitutive behavior described above, as well as to assign integration-point specific material data, based on injection molding simulations performed using Moldex3D [74]. To avoid some practical problems associated with large numbers of section- and material assignments, the constitutive parameters are set for each integration point directly in the constitutive model. The effect of this is that only a single material definition is used, which contains all of the fiber orientations and material data. This circumvents performance issues related to large numbers of material definitions which are present in several commercial finite element codes.

### 4.3 Numerical/analytical method (Papers IV & V)

Building finite element models of complex microstructures is associated with several problems. Based on micrographs in 2D, or image stacks in 3D, the input is on the form of either pixels or voxels, where phase boundaries are inherently "jagged". By smoothing such data sets, not only is the experimental data distorted, but without using more sophisticated discretization methods, the nodal connectivity between phases is typically lost. This leads to large amounts of manual- and labor intensive pre-processing. Another issue associated with such datasets is that the amount of information might be too large to fully utilize, depending on the available processing power. These problems were addressed in Papers IV & V, by the development of a pixel/voxel-based semi-multiscale method, with the intent of enabling a simple and rational consideration of large such data sets on the macro-scale.

The main idea of the method is to split the imaging data set into subdomains, which are used to build numerical models. These numerical models are homogenized individually using phase properties based on the local pixel/voxel intensity. The homogenized properties are then mapped to a reduced finite element model, i.e. where the number of elements is lower than the initial number of pixels/voxels. Julia [75] was used to implement this method for arbitrary micrographs and image stacks, containing any number of phases. The flowchart in Fig. 4.2 provides an overview, while the splitting, meshing and mapping operation is illustrated for 2D in Fig. 4.3, and for 3D in Fig. 4.4.

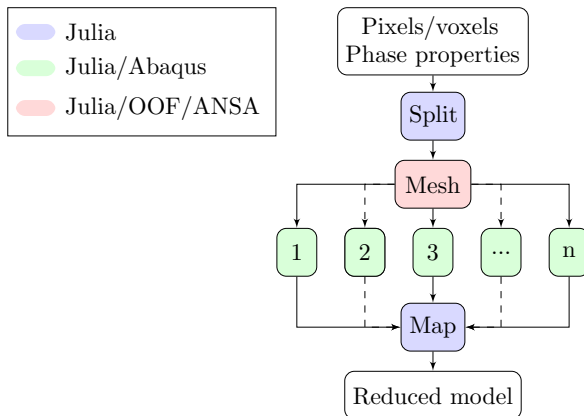


Figure 4.2: Implementation flowchart. Pixels or voxels together with phase properties are used as input. The imaging data is split into  $n$  subdomains which are discretized (red) using either Julia [75], OOF2/3D [76] or ANSA [77]. Homogenization (green) of each subdomain is performed using Julia or Abaqus [70] with EasyPBC [71], and the effective properties are mapped back to a reduced mesh of the same physical dimensions as the original micrograph.



In Paper IV, this method is described and evaluated for 2D problems, using different discretization and homogenization strategies. Artificial micrographs of finite plates containing circular holes, and an experimentally obtained SEM micrograph describing a complex aluminum microstructure were analysed. Pixel-wise discretization is compared to when phase boundaries are partially or fully smoothed, with respect to errors in stress and effective constitutive properties. Two homogenization strategies were investigated, one numerical where Periodic Boundary Conditions (PBC) are applied to each subdomain, and one semi-analytical where averaged Hashin-Shtrikman bounds are calculated based on fractions determined via pixel summation using Eqs. 3.27 and 3.28.

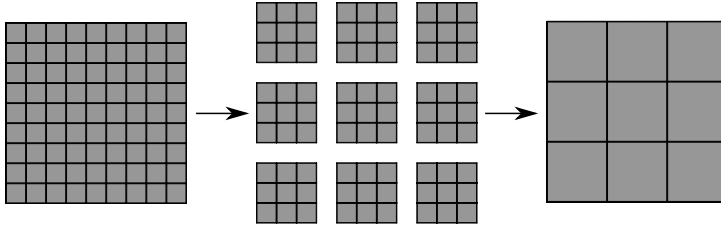


Figure 4.3: Input micrograph containing  $9 \cdot 9$  pixels (left) split into  $3 \cdot 3$  subdomains (middle) where each pixel is represented by one element. Effective properties are computed for each subdomain which are then mapped back to a reduced model containing  $3 \cdot 3$  elements (right).

In Paper V, the same method was extended to 3D problems, and evaluated using the same numerical and semi-analytical homogenization methods. Errors in stress concentration and predicted effective elastic constitutive model parameters were estimated using artificial image stacks containing spherical holes, by comparison to analytical solutions. Finally, the method was applied to a complex high-resolution shrinkage porosity, retrieved from an aluminum alloy image stack. A voxel-wise discretization strategy was used for all analyses, except for a smooth reference model of the aluminum shrinkage porosity.

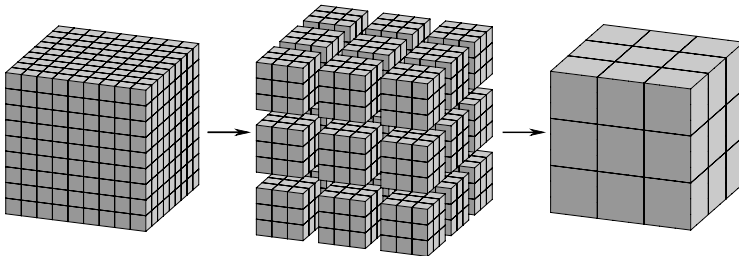


Figure 4.4: Input image stack containing  $9 \cdot 9 \cdot 9$  voxels (left) split into  $3 \cdot 3 \cdot 3$  subdomains (middle) where each voxel is represented by one element. Effective properties are computed for each subdomain which are then mapped back to a reduced model of  $3 \cdot 3 \cdot 3$  elements (right).



# Chapter 5

## Conclusions

This chapter summarizes, and elaborates on the conclusions from the appended papers. The purpose and aim of this work was to develop and evaluate methods for the determination of heterogeneous constitutive model parameters, based on microstructural variations, caused by the manufacturing process. So that their influence on component performance can be better understood, in the context of simulation-driven industrial product development. By decreasing material modeling errors, industrially manufactured components have the potential to become further optimized with respect to multiple performance metrics such as weight, cost and environmental impact.

### 5.1 Empirical method, cast flake graphite iron (Papers I & II)

The following objectives were defined in Section 1.3:

*Evaluate the influence of material modeling errors for sand cast lamellar graphite iron components, such as the neglect of:*

- *Heterogeneous material behavior*
- *Residual stresses*
- *Difference between tensile and compressive behavior*
- *Temperature dependency*

In Papers I & II, empirical models for thermo- mechanical and physical material behavior were created by optimization towards experimental measurements and literature data, for a flake graphite cast iron cylinder head. These models depend on the solidification time, as predicted by casting process simulations. Static and thermal analyses were performed using these models, with varying levels of detail and distribution of material data. The stress- and temperature fields of simplified numerical models were then compared against

a reference model containing all of the available material data, i.e. the presented error is with respect to numerical reference models. Figs. 5.1a and 5.1b illustrate the applied static, and transient thermal load-cases respectively.

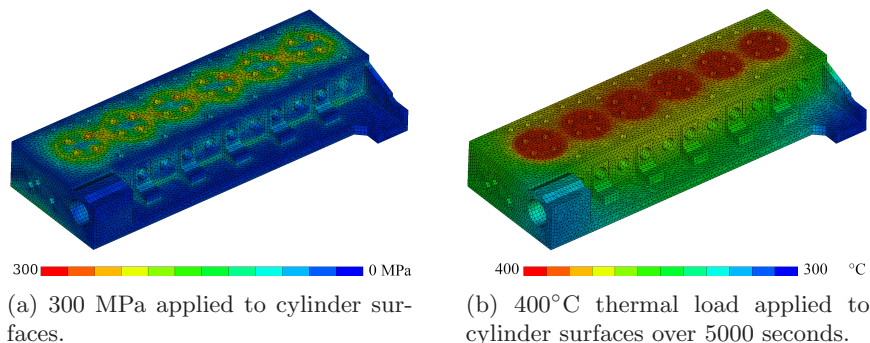


Figure 5.1: Load-cases used in cylinder head evaluations.

By neglecting process-induced heterogeneous constitutive model parameters, residual stresses, the compressive behavior, or the temperature dependency of the material one by one, or several at once, "non-trivial" errors were found. Non-trivial in the sense that errors would not have been easily predicted without performing the actual comparison. More specifically, the simplifications did not lead to simple over- or under-estimation of stress or temperature, but a combination of both in different regions of the component, with no obvious pattern relative to the applied load. Also, in some cases, errors due to one or two variable neglects counteracted a third. Where the errors were classified as "predictable", there was a clear relationship between the error and the applied load. As an example, the error increases with distance from the applied thermal load when neglecting heterogeneous constitutive model parameters in the transient thermal analysis. In summary, the result of neglecting these material-related aspects for different analysis types and load-cases were:

### Static mechanical analysis (load: 300 MPa)

- Heterogeneous material behavior: small, non-trivial errors of 12 MPa
- Residual stresses: large, non-trivial errors of 128 MPa
- Compressive properties: large, non-trivial errors of 40 MPa (Fig. 5.2a)
- Temperature dependency: large, non-trivial errors of 57 MPa

### Transient thermal analysis (load: 400°C over 5000 s)

- Heterogeneous material behavior: negligible, non-trivial errors of 0.29°C (Fig. 5.2b)

- Temperature dependency: large, predictable errors of  $51^{\circ}\text{C}$

Fig. 5.2a illustrates the effective von Mises stress field error retrieved by neglecting the compressive material properties, for the static load-case. Fig. 5.2b illustrates the error in temperature distribution by neglecting process-induced heterogeneous material properties, for the thermal load-case. Both of which illustrate "non-trivial" errors with respect to the applied load, in the sense that they are not easily predictable without direct comparison.

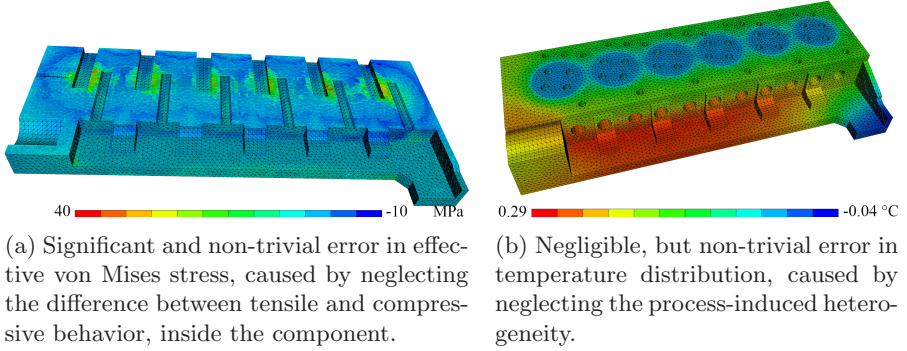


Figure 5.2: Static mechanical and transient thermal evaluation of cast iron cylinder head.

While the use of numerical reference models in Papers I & II for e.g. residual stresses decreases the generality of the numerical results, as opposed to comparisons against experimentally verified data, it is still possible to conclude that non-trivial, and thus potentially dangerous errors could occur in component-level simulations by disregarding even small differences in material behavior.

## 5.2 Statistical method, injection molded short GFRPs (Paper III)

The following objective was defined in Section 1.3:

*Develop a method for the consideration of the heterogeneous fiber orientation in structural analyses of injection molded short glass fiber reinforced composites*

In Paper III, analytical homogenization and statistical orientation averaging methods were used together with an anisotropic non-linear constitutive model, to describe the material behavior of injection molded short Glass Fiber Reinforced Plastics (GFRP), in terms of the fiber orientation. The constitutive model was implemented in the commercial finite element codes LS-DYNA

[73] and Abaqus [70], allowing integration-point specific and fiber orientation dependent constitutive model parameters, based on the results of injection molding simulations, using only one material definition. A optimization-based method was applied to determine the constitutive model parameters, where numerical and experimental material tests were performed using samples containing different, but approximately homogeneous fiber orientations.

The developed method was demonstrated by optimizing the anisotropic elastic and plastic constitutive response of a composite material reinforced with 50 wt.% short glass fibers. The results can be seen in Fig. 5.3, where the constitutive model parameters have been optimized against experimental tensile test results for both  $0^\circ$ ,  $45^\circ$  and  $90^\circ$  fiber orientations simultaneously. It should be noted that the behavior of all three simulations depend on each other, since the fiber orientation in the tensile specimens are only approximately homogeneous.

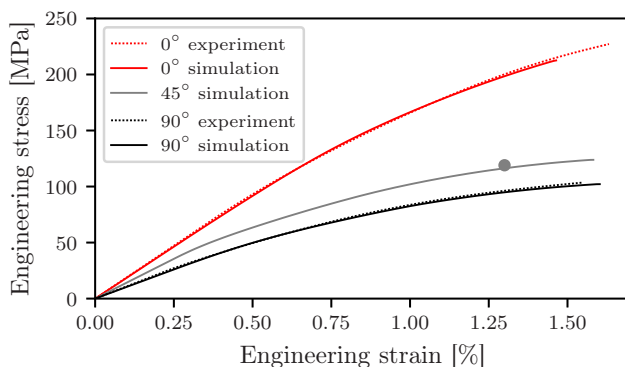


Figure 5.3: Demonstration of the proposed constitutive models ability to capture the behavior of three different fiber orientations, using a material with 50 wt.% glass fibers. The gray dot represents an approximation for where the  $45^\circ$  fiber orientation could be located, based on a material with 30 wt.% fibers.

While no component-level validation was performed within the scope of this study, it can still be concluded that the proposed method and constitutive model successfully captures the anisotropic and non-linear behavior of the studied material, for the investigated geometry and loading conditions. With further validation, the method could be a useful tool in capturing complex phenomena like the through-thickness variation of the fiber orientation, allowing engineers to evaluate the influence which this has on component performance. By also considering the results and conclusions from Papers I & II for much smaller differences in material behavior, it is likely that large performance gains could be made by applying the proposed method to component-level simulations in simulation-driven product development.

### 5.3 Numerical/analytical method, cast aluminum (Papers IV & V)

The following objective was defined in Section 1.3:

*Develop and evaluate a method for the generation of reduced numerical microstructure models, based on 2D micrographs or 3D image stacks*

In Papers IV (2D) & V (3D), a semi-multiscale modeling methodology for elastic problems was developed. A reduced finite element model is generated from a pixel- or voxel-representation of a complex microstructure, by using subdomains which are homogenized numerically using Periodic Boundary Conditions (PBC), or semi-analytically using averaged Hashin-Shtrikman bounds. The method was evaluated using both artificial and experimentally obtained imaging data. The artificial data describes finite plates containing large circular holes, and finite cubes containing large spherical holes, of varying radius up to a 0.9 width/diameter ratio. These models were intended to represent worst-case conditions for what could occur locally in individual subdomains, during the reduction of complex microstructures. The experimentally obtained imaging data on the other hand, represents applications in the form of cast aluminum alloy microstructures, containing multiple solid phases and porosity.

The method was evaluated by computing the relative error

$$\Delta \bullet = \frac{\bullet - \bullet_r}{\bullet_r} \cdot 100 [\%], \quad (5.1)$$

where  $\bullet_r$  represents a reference solution for the quantity  $\bullet$ , which could be stiffness  $E$ , Poisson's ratio  $\nu$ , principal stress  $\sigma_1$  or a stress concentration factor  $K_t$ . By evaluating artificial imaging data, the following errors were found for

#### Large circular holes in finite 2D plates

- Numerical method

$$\Delta E \leq 23\%$$

$$\Delta \nu \leq 75\%$$

$$\Delta \sigma_1 \leq 55\%$$

- Semi-analytical method

$$\Delta E \leq 63\%$$

$$\Delta \nu \leq 175\%$$

$$\Delta \sigma_1 \leq 55\%$$

#### Large spherical holes in finite 3D domains

- Numerical method

$$\Delta E \leq 4\%$$

$$\Delta \nu \leq 7\%$$

$$\Delta K_t \leq 75\%$$

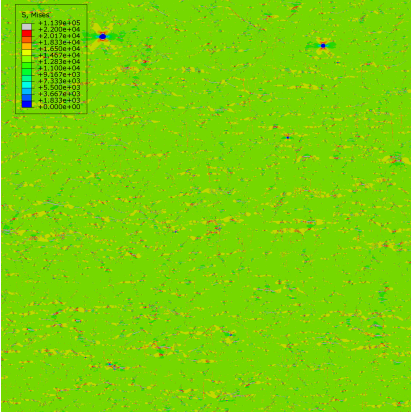
- Semi-analytical method

$$\Delta E \leq 55\%$$

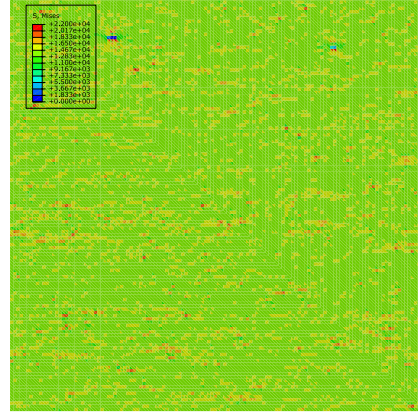
$$\Delta \nu \leq 15\%$$

$$\Delta K_t \leq 75\%$$

Next, the method was evaluated by using 2D and 3D imaging data obtained via Scanning Electron Microscopy (SEM) and Computed Tomography (CT). The resulting stress fields for the 2D evaluation is illustrated in Figs. 5.4a, 5.4b, while the 3D evaluation is illustrated in Figs. 5.5a and 5.5b.

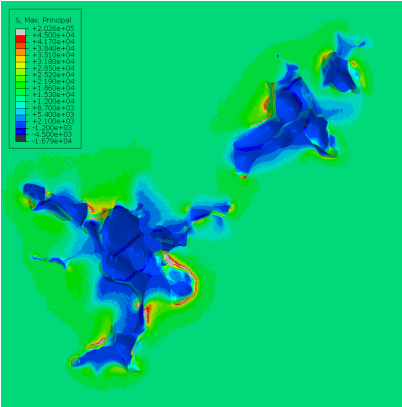


(a) Reference 2D model, where each pixel of the original aluminum micrograph has been discretized using two first order triangular elements per pixel. (30 000 000 elements)

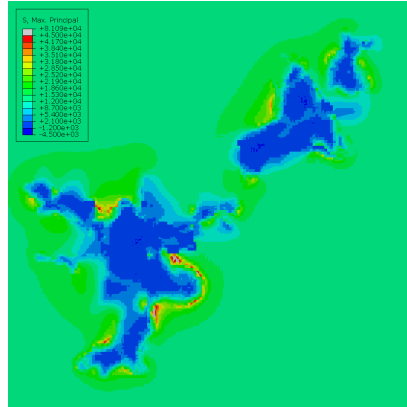


(b) Reduced model, where the number of elements in the reference model has been decreased by 99.89%, to 32 768 triangular elements, using numerical homogenization and  $128^2$  subdomains.

Figure 5.4: Effective stress after uni-axial loading of 2D aluminum plate.



(a) Reference 3D model cross-section, manually pre-processed and discretized using 48 357 618 elements. Cubical volume containing a large shrinkage porosity with a complex shape.

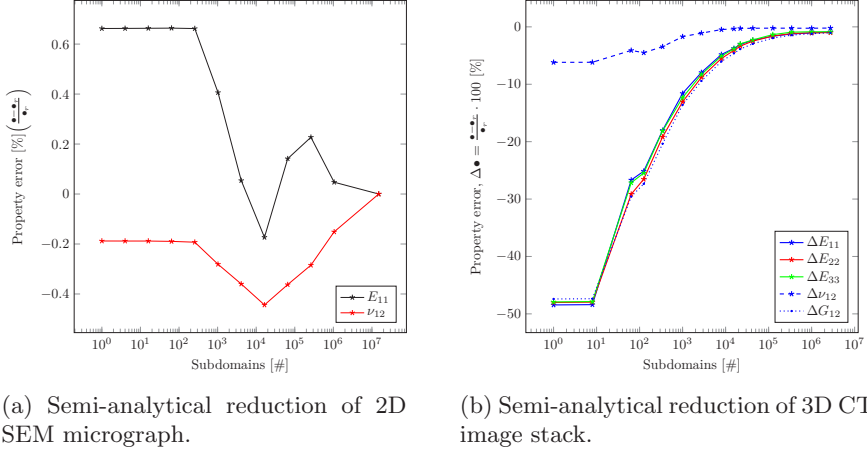


(b) Reduced model, where the number of elements in the reference model has been decreased by 94.32%, to 2 744 000 elements and subdomains, using semi-analytical homogenization.

Figure 5.5: Principal stress after uni-axial loading of 3D aluminum cube.



The effective elastic properties of the reduced models were then evaluated as a function of the number of subdomains. The resulting material property errors are illustrated in Fig. 5.6a for 2D, and in Fig. 5.6b for 3D.



(a) Semi-analytical reduction of 2D SEM micrograph. (b) Semi-analytical reduction of 3D CT image stack.

Figure 5.6: Material property errors for different numbers of subdomains.

From the evaluation of artificial imaging data, it could be concluded that the numerical method outperforms the semi-analytical one with respect to estimating constitutive parameters. However, high local errors in both stress and constitutive model properties were seen using both methods. The drawback of the numerical method is that the computational time becomes unreasonably high for larger problems. This can be resolved by applying the more computationally efficient semi-analytical homogenization method, which has an accuracy similar to the numerical method for larger numbers of subdomains. The drawback of the semi-analytical method is that it is inaccurate for low numbers of subdomains, where the elastic properties may be under-estimated by up to 55%. Additionally, both homogenization methods under-estimate local stress concentrations for smaller numbers of subdomains. For these reasons, it is suggested to use as many subdomains as one can afford given the available memory and processing power, and to select the homogenization method based on the above recommendations.

From the evaluation of experimentally obtained imaging data, it could be concluded that while local errors may be high, the method was still able to accurately reduce the 2D model by 99.89% and the 3D model by 94.32%, with errors lower than 1% for the elastic constitutive parameters. Characteristics of the stress-field such as the location of stress concentrations remained, however the magnitude of the stress was under-estimated by approximately one order of magnitude when compared to a traditionally pre-processed finite element model.

The presented methodology is a first step towards reducing pixel- and voxel-representations of complex microstructures to a size where they may be included in component level simulations. One application of this might be the inclusion of a porosity distribution retrieved from a casting process simulation, or via X-ray based imaging methods applied on a production line. This would allow engineers to consider the influence this might have on component performance. The method could also be used as a pre-processing step in the creation of more advanced numerical models, where the number of elements needs to be kept low while still containing a large amount of heterogeneous material data.

# Chapter 6

## Future work

The research which is summarized in this thesis has spawned multiple ideas for future work. In this chapter, suggestions are given for improvements and extensions to the methodologies in the appended papers.

### Papers I & II

The method described in the first two papers is applicable to any type of manufacturing process which introduces a heterogeneous microstructure in the produced component. By performing initial simulations of the manufacturing process together with material characterization, heterogeneous model parameters can be generated for macro-scale finite element simulations in a two-step approach. A few examples of this could be the consideration of the grain structure from forging, anisotropic behavior caused by the draw-direction in thermo-forming, flow induced fiber orientation in fiber reinforced composites, porosity or other microstructural imperfections in cast components, or the heterogeneous constitutive behavior caused by additive manufacturing processes. Furthermore, the method could be extended with multi-axial and/or dynamic material testing combined with more sophisticated constitutive models to provide a more general description of the heterogeneous constitutive behavior in structural analyses.

### Paper III

The approach taken in the third paper could be further improved, extended and validated. A more general formulation of anisotropic fiber orientation dependent plasticity, including a pressure-dependent yield criterion would improve the validity of the proposed constitutive model with respect to fiber reinforced plastics. Rate dependency, damage mechanisms, etc. could be included to further improve the predictive capabilities of the model. While the non-linear and anisotropic behavior of the investigated material was successfully captured using optimization against numerical models, the actual fiber

orientation in the tensile specimens is unknown. Also, component-level validation would be necessary before confidently applying the method to industrial problems. Following larger efforts in validation, shape/topology and process-variable optimization could be applied to minimize the difference between the local fiber orientation and the principal stress vector for each material point, further optimizing the material utilization in fiber reinforced parts under in-use conditions.

## **Papers IV & V**

While the method described in the last two papers significantly reduces the complexity of building finite element models of complex microstructures, a more sophisticated discretization method is required for accurate stress predictions. Level-set based methods could be applied to create numerical models of the microstructure with smooth phase boundaries. Adaptive mesh-reduction could be applied to reduce the number of neighboring elements with similar constitutive model parameters, to reduce memory requirements. The performance of the numerical homogenization method could be increased significantly by optimizing the implementation, alternatively by using a different numerical method such as e.g. finite differences. Furthermore, a computationally efficient description of the non-linear subdomain response, while not trivial, would take the method to the next level. This might be achievable by using e.g. artificial neural networks with physical constraints in the training data set, or other data-driven methods. The initial idea was to use the proposed method in support of macro-scale fatigue life predictions, allowing consideration of the micro-scale porosity contents. The proposed method is a first step in this direction, however further progress would also require an approximation of the porosity distribution from a casting process simulation, or simulations of microstructure growth, unless retrieved via X-ray based 2D or 3D imaging methods. In this context, it should also be noted that the mechanisms which control porosity formation in metal casting are still not fully understood. In future works, the simplicity and performance of the method should also be compared to other available model reduction methods, including available commercial software.

# Bibliography

- [1] A. Tolk, “Learning Something Right from Models That Are Wrong: Epistemology of Simulation,” in *Concepts and methodologies for modeling and simulation*, pp. 87–106, springer, 2015.
- [2] M. Hofmann, “On the Complexity of Parameter Calibration in Simulation Models,” *The Journal of Defense Modeling and Simulation: Applications, Methodology, Technology*, vol. 2, no. 4, pp. 217–226, 2005.
- [3] G. E. P. Box and N. R. Draper, *Empirical Model-Building and Response Surfaces*. Wiley, 1987.
- [4] L. E. Schwer, “An overview of the ptc 60/v&v 10: guide for verification and validation in computational solid mechanics,” *Engineering with Computers*, vol. 23, pp. 245–252, Dec 2007.
- [5] Q. G. Wang, D. Apelian, and D. A. Lados, “Fatigue behavior of A356-T6 aluminum cast alloys. Part I. Effect of casting defects,” *Journal of Light Metals*, vol. 1, no. 1, pp. 73–84, 2001.
- [6] Q. G. Wang, D. Apelian, and D. A. Lados, “Fatigue behavior of A356/357 aluminum cast alloys. Part II - Effect of microstructural constituents,” *Journal of Light Metals*, vol. 1, no. 1, pp. 85–97, 2001.
- [7] K. Salomonsson and A. E. W. Jarfors, “Three-Dimensional Microstructural Characterization of Cast Iron Alloys for Numerical Analyses Kent Salomonsson,” *Materials Science Forum*, vol. 925, pp. 427–435, 2018.
- [8] A. Reardon, *Metallurgy for the Non-Metallurgist*. ASM International, 2 ed., 2011.
- [9] A. Diószegi, V. Fourlakidis, and R. Lora, “Austenite dendrite morphology in lamellar graphite iron,” *International Journal of Cast Metals Research*, vol. 28, no. 5, pp. 310–317, 2015.
- [10] L. Elmquist and A. Diószegi, “Shrinkage porosity and its relation to solidification structure of grey cast iron parts,” *International Journal of Cast Metals Research*, vol. 23, no. 1, pp. 44–50, 2010.

- [11] L. Collini, G. Nicoletto, and R. Konečná, “Microstructure and mechanical properties of pearlitic gray cast iron,” *Materials Science and Engineering A*, vol. 488, no. 1-2, pp. 529–539, 2008.
- [12] A. Diószegi, V. Furlakidis, and I. L. Svensson, “Microstructure and tensile properties of grey cast iron,” *Micro*, pp. 2–35, 2004.
- [13] T. Sjögren and I. L. Svensson, “Modelling the effect of graphite morphology on the modulus of elasticity in cast irons,” *International Journal of Cast Metals Research*, vol. 17, no. 5, pp. 271–279, 2004.
- [14] T. Sjögren and I. L. Svensson, “The effect of graphite fraction and morphology on the plastic deformation behavior of cast irons,” in *Metallurgical and Materials Transactions A: Physical Metallurgy and Materials Science*, vol. 38, pp. 840–847, 2007.
- [15] V. Furlakidis, V. L. Diaconu, and A. Diószegi, “Effects of Carbon Content on the Ultimate Tensile Strength in Gray Cast Iron,” *Materials Science Forum*, vol. 649, pp. 511–516, 2010.
- [16] V. Furlakidis and A. Diószegi, “A generic model to predict the ultimate tensile strength in pearlitic lamellar graphite iron,” *Materials Science and Engineering A*, vol. 618, pp. 161–167, 2014.
- [17] T. Sjögren and H. Svensson, “Study of the eutectoid transformation in grey cast irons and its effect on mechanical properties,” *Key Engineering Materials*, vol. 457, pp. 157–162, 2011.
- [18] C. Maraveas, Y. C. Wang, T. Swailes, and G. Sotiriadis, “An experimental investigation of mechanical properties of structural cast iron at elevated temperatures and after cooling down,” *Fire Safety Journal*, vol. 71, no. 1, pp. 340–352, 2015.
- [19] H. Altenbach, G. B. Stoychev, and K. N. Tushtev, “On elastoplastic deformation of grey cast iron,” *International Journal of Plasticity*, vol. 17, no. 5, pp. 719–736, 2001.
- [20] J. K. Holmen, B. H. Frodal, O. S. Hopperstad, and T. Børvik, “Strength differential effect in age hardened aluminum alloys,” *International Journal of Plasticity*, vol. 99, no. 7491, pp. 144–161, 2017.
- [21] M. A. Akinpelu, S. O. Odeyemi, O. S. Olafusi, and F. Z. Muhammed, “Evaluation of splitting tensile and compressive strength relationship of self-compacting concrete,” *Journal of King Saud University - Engineering Sciences*, 2018.
- [22] S. Sankaranarayanan, S. Jayalakshmi, and M. Gupta, “Effect of addition of mutually soluble and insoluble metallic elements on the microstructure, tensile and compressive properties of pure magnesium,” *Materials Science and Engineering A*, vol. 530, no. 1, pp. 149–160, 2011.

- [23] D. Holmgren, A. Diószegi, and I. L. Svensson, “Effects of carbon content and solidification rate on thermal conductivity of grey cast iron,” *China Foundry*, vol. 4, no. 3, pp. 210–214, 2007.
- [24] D. Holmgren and I. L. Svensson, “Thermal conductivity-structure relationships in grey cast iron,” *International Journal of Cast Metals Research*, vol. 18, no. 6, pp. 321–330, 2013.
- [25] J. Jansson, J. Olofsson, and K. Salomonsson, “On the use of heterogeneous thermomechanical and thermophysical material properties in finite element analyses of cast components,” *IOP Conference Series: Materials Science and Engineering*, vol. 529, no. 1, 2019.
- [26] M. Nciri, D. Notta-Cuvier, F. Lauro, F. Chaari, Y. Maalej, and B. Zouari, “Modelling and characterisation of dynamic behaviour of short-fibre-reinforced composites,” *Composite Structures*, vol. 160, pp. 516–528, 2017.
- [27] B. Mouhmid, A. Imad, N. Benseddiq, S. Benmedakhène, and A. Maazouz, “A study of the mechanical behaviour of a glass fibre reinforced polyamide 6,6: Experimental investigation,” *Polymer Testing*, vol. 25, no. 4, pp. 544–552, 2006.
- [28] D. Valentin, F. Paray, and B. Guetta, “The hygrothermal behaviour of glass fibre reinforced Pa66 composites: A study of the effect of water absorption on their mechanical properties,” *Journal of Materials Science*, vol. 22, no. 1, pp. 46–56, 1987.
- [29] S. Mortazavian and A. Fatemi, “Effects of fiber orientation and anisotropy on tensile strength and elastic modulus of short fiber reinforced polymer composites,” *Composites Part B: Engineering*, vol. 72, pp. 116–129, 2015.
- [30] E. W. Liang and V. K. Stokes, “Mechanical properties of injection-molded short-fiber thermoplastic composites. Part 1 : The elastic moduli and strengths of glass-filled poly(butylene terephthalate),” *Polymer Composites*, vol. 26, no. 4, pp. 428–447, 2005.
- [31] J. L. Thomason, “The influence of fibre properties of the performance of glass-fibre-reinforced polyamide 6,6,” *Composites Science and Technology*, vol. 59, no. 16, pp. 2315–2328, 1999.
- [32] H. W. Wang, H. W. Zhou, L. L. Gui, H. W. Ji, and X. C. Zhang, “Analysis of effect of fiber orientation on Young’s modulus for unidirectional fiber reinforced composites,” *Composites Part B: Engineering*, vol. 56, pp. 733–739, 2014.
- [33] A. Andriyana, N. Billon, and L. Silva, “Mechanical response of a short fiber-reinforced thermoplastic: Experimental investigation and continuum mechanical modeling,” *European Journal of Mechanics, A/Solids*, vol. 29, no. 6, pp. 1065–1077, 2010.

- [34] M. De Monte, E. Moosbrugger, and M. Quaresimin, "Influence of temperature and thickness on the off-axis behaviour of short glass fibre reinforced polyamide 6.6 - Cyclic loading," *Composites Part A: Applied Science and Manufacturing*, vol. 41, no. 10, pp. 1368–1379, 2010.
- [35] J. Jansson, T. Gustafsson, K. Salomonsson, J. Olofsson, J. Johansson, P. Appelsved, and M. Palm, "An Anisotropic Non-linear Material Model for Glass Fibre Reinforced Plastics," *Composite Structures*, vol. 195, no. April, pp. 1–8, 2018.
- [36] P. R. Goulart, J. E. Spinelli, W. R. Osório, and A. Garcia, "Mechanical properties as a function of microstructure and solidification thermal variables of Al-Si castings," *Materials Science and Engineering A*, vol. 421, no. 1-2, pp. 245–253, 2006.
- [37] Q. Wang, "Microstructural Effects on the Tensile and Fracture Behavior of Aluminum Casting Alloys A356 / 357," *Metallurgical and Materials Transactions A*, vol. 34, no. December, pp. 2887–2899, 2003.
- [38] F. Lasagni, A. Lasagni, E. Marks, C. Holzapfel, F. Mücklich, and H. P. Degischer, "Three-dimensional characterization of 'as-cast' and solution-treated AlSi12(Sr) alloys by high-resolution FIB tomography," *Acta Materialia*, vol. 55, no. 11, pp. 3875–3882, 2007.
- [39] E. Ogris, A. Wahlen, H. Lüchinger, and P. J. Uggowitzer, "On the silicon spheroidization in Al-Si alloys," *Journal of Light Metals*, vol. 2, no. 4, pp. 263–269, 2002.
- [40] A. K. Gupta, B. H. K. H. K. Saxena, S. N. Twari, S. L. Malhotra, S. N. Tiwari, S. L. Malhotra, S. N. Twari, and S. L. Malhotra, "Review: Pore formation in cast metals and alloys," *Journal of Materials Science*, vol. 27, no. 4, pp. 853–862, 1992.
- [41] P. D. Lee, J. Wang, and M. Li, "Coupling in-situ observations and microscale modeling to predict pore and Fe-rich intermetallic formation during the solidification of Al-Si-Cu-Fe alloys," *Proceedings from the 12th International Conference on Modeling of Casting, Welding, and Advanced Solidification Processes*, pp. 87–99, 2009.
- [42] C. Puncreobutr, P. D. Lee, R. W. Hamilton, and A. B. Phillion, "Quantitative 3D characterization of solidification structure and defect evolution in Al alloys," *Jom*, vol. 64, no. 1, pp. 89–95, 2012.
- [43] C. Puncreobutr, P. D. Lee, K. M. Kareh, T. Connolley, J. L. Fife, and A. B. Phillion, "Influence of Fe-rich intermetallics on solidification defects in Al-Si-Cu alloys," *Acta Materialia*, vol. 68, pp. 42–51, 2014.
- [44] L. Salvo, M. Pana, M. Suéry, M. Dimichiel, O. Nielsen, and D. Bernard, "Fast X-ray tomography investigation of solidification microstructure and



- defect formation in aluminium alloys,” *Modeling of Casting, Welding and Advanced Solidification Processes - XI*, vol. 1, 2006.
- [45] S. Terzi, J. A. Taylor, Y. H. Cho, L. Salvo, M. Suéry, E. Boller, and A. K. Dahle, “In situ study of nucleation and growth of the irregular  $\alpha$ -Al/ $\beta$ -Al<sub>5</sub>FeSi eutectic by 3-D synchrotron X-ray microtomography,” *Acta Materialia*, vol. 58, no. 16, pp. 5370–5380, 2010.
  - [46] P. Mikolajczak and L. Ratke, “Interplay Between Melt Flow and the 3D Distribution and Morphology of Fe-Rich Phases in AlSi Alloys,” *Metallurgical and Materials Transactions A: Physical Metallurgy and Materials Science*, vol. 46, no. 3, pp. 1312–1327, 2014.
  - [47] J. M. Yu, N. Wanderka, A. Rack, R. Daudin, E. Boller, H. Markötter, A. Manzoni, F. Vogel, T. Arlt, I. Manke, and J. Banhart, “Formation of intermetallic  $\delta$  phase in Al-10Si-0.3Fe alloy investigated by in-situ 4D X-ray synchrotron tomography,” *Acta Materialia*, vol. 129, pp. 194–202, 2017.
  - [48] G. Nicoletto, G. Anzelotti, and R. Konečná, “X-ray computed tomography vs. metallography for pore sizing and fatigue of cast Al-alloys,” in *Procedia Engineering*, vol. 2, pp. 547–554, 2010.
  - [49] L. Ceschini, I. Boromei, A. Morri, S. Seifeddine, and I. L. Svensson, “Microstructure, tensile and fatigue properties of the Al-10%Si-2%Cu alloy with different Fe and Mn content cast under controlled conditions,” *Journal of Materials Processing Technology*, vol. 209, no. 15-16, pp. 5669–5679, 2009.
  - [50] Q. G. Wang and C. H. Caceres, “On the strain hardening behaviour of Al-Si-Mg casting alloys,” *Materials Science and Engineering: A*, vol. 236, pp. 106–109, 1997.
  - [51] M. D. Dighe, A. M. Gokhale, and M. F. Horstemeyer, “Effect of Loading Condition and Stress State on Damage Evolution of Silicon Particles in an Al-Si-Mg-Base Cast Alloy,” *Metallurgical and Materials Transactions A*, vol. 33, pp. 555–565, mar 2000.
  - [52] J. F. Su, X. Nie, and V. Stoilov, “Characterization of fracture and debonding of Si particles in AlSi alloys,” *Materials Science and Engineering A*, vol. 527, pp. 7168–7175, oct 2010.
  - [53] X. Cao and J. Campbell, “The nucleation of Fe-rich phases on oxide films in Al-11.5 Si-0.4 Mg cast alloys,” *Metall. Mater. Trans. A*, vol. 34, no. July, pp. 1409–1420, 2003.
  - [54] J. Campbell, *Complete Casting Handbook: Metal Casting Processes, Techniques and Design*. Oxford, UK ; Waltham, MA: Elsevier Butterworth-Heinemann, 1st ed.. ed., 2015.

- [55] F. L.Liu, “Effect of inclusions on the tensile properties of Al-7Si-0,35Mg (A356.2) aluminium casting alloy .pdf,” *Journal of Materials Science*, vol. 33, no. 9, pp. 2269–2281, 1998.
- [56] Y. X. Gao, J. Z. Yi, P. D. Lee, and T. C. Lindley, “The effect of porosity on the fatigue life of cast aluminium-silicon alloys,” *Fatigue and Fracture of Engineering Materials and Structures*, vol. 27, no. 7, pp. 559–570, 2004.
- [57] I. Koutiri, D. Bellett, F. Morel, L. Augustins, and J. Adrien, “High cycle fatigue damage mechanisms in cast aluminium subject to complex loads,” *International Journal of Fatigue*, vol. 47, pp. 44–57, 2013.
- [58] M. K. Surappa, E. Blank, and J. C. Jaquet, “Scripta Metall. et Mater.,,” *Effect of Macro-porosity on the Strength and Ductility of Cast Al-7Si-0.3 Mg alloy*, vol. 20, pp. 1281–1286, sep 1986.
- [59] S. Dezecot, V. Maurel, J.-Y. Buffiere, F. Szymtka, and A. Koster, “3D characterization and modeling of low cycle fatigue damage mechanisms at high temperature in a cast aluminum alloy,” *Acta Materialia*, vol. 123, pp. 24–34, 2017.
- [60] H. Mughrabi, “Damage mechanisms and fatigue lives: From the low to the very high cycle regime,” in *Procedia Engineering*, vol. 55, pp. 636–644, Elsevier B.V., 2013.
- [61] V.-D. Le, F. Morel, D. Bellett, N. Saintier, and P. Osmond, “Multiaxial high cycle fatigue damage mechanisms associated with the different microstructural heterogeneities of cast aluminium alloys,” *Materials Science and Engineering: A*, vol. 649, pp. 426–440, 2016.
- [62] C. S. Man and M. Huang, “A simple explicit formula for the Voigt-Reuss-Hill average of elastic polycrystals with arbitrary crystal and texture symmetries,” *Journal of Elasticity*, vol. 105, no. 1-2, pp. 29–48, 2011.
- [63] Z. Hashin and S. Shtrikman, “A variational approach to the theory of the elastic behaviour of multiphase materials,” *Journal of the Mechanics and Physics of Solids*, vol. 11, no. 2, pp. 127–140, 1963.
- [64] J. D. Eshelby, “The determination of the elastic field of an ellipsoidal inclusion in an anisotropic medium,” *Mathematical Proceedings of the Cambridge Philosophical Society*, vol. 81, no. 2, pp. 283–289, 1977.
- [65] Y. Benveniste, “A new approach to the application of Mori - Tanaka’s theory in composite materials,” 1987.
- [66] T. Mori and K. Tanaka, “Average stress in matrix and average elastic energy of materials with misfitting inclusions,” *Acta Metallurgica*, vol. 21, pp. 571–574, may 1973.
- [67] T. Mura, “Micromechanics of defects in Solids,” 1987.

- [68] R. Pyrz, “The Mori-Tanaka stiffness tensor : diagonal symmetry, complex fibre orientations and non-dilute volume fractions,” *Mechanics of Materials*, vol. 33, pp. 531–544, 2001.
- [69] Z. Xia, Y. Zhang, and F. Ellyin, “A unified periodical boundary conditions for representative volume elements of composites and applications,” *International Journal of Solids and Structures*, vol. 40, no. 8, pp. 1907–1921, 2003.
- [70] Dassault Systèmes Simulia Corp., “Abaqus CAE 2021,” 2021.
- [71] S. L. Omairey, P. D. Dunning, and S. Sriramula, “Development of an ABAQUS plugin tool for periodic RVE homogenisation,” *Engineering with Computers*, vol. 35, no. 2, pp. 567–577, 2019.
- [72] S. G. Advani and C. L. Tucker, “The Use of Tensors to Describe and Predict Fiber Orientation in Short Fiber Composites,” *Journal of Rheology*, vol. 31, no. 8, pp. 751–784, 1987.
- [73] Livermore Software Technology, “LS-DYNA,” 2018.
- [74] CoreTech System Co., Ltd., “Moldex3D,” 2018.
- [75] J. Bezanson, A. Edelman, S. Karpinski, and V. B. Shah, “Julia: A fresh approach to numerical computing,” *SIAM review*, vol. 59, no. 1, pp. 65–98, 2017.
- [76] V. R. Coffman, A. C. Reid, S. A. Langer, and G. Dogan, “OOF3D: An image-based finite element solver for materials science,” *Mathematics and Computers in Simulation*, vol. 82, no. 12, pp. 2951–2961, 2012.
- [77] BETA CAE Systems International, Inc., “Ansa Preprocessor v20.1.6,” 2021.

# Multiscale Constitutive Modeling of Heterogeneous Engineering Materials

This work deals with different methods used to determine heterogeneous constitutive model parameters for macro-scale finite element models, based on microstructural variations, caused by the manufacturing process. These methods could be applied to decrease modeling errors associated with the material behavior, improving the predictive capabilities of structural analyses in simulation-driven industrial product development. By providing engineers with more sophisticated tools and methods which lets them consider the complex relationships between the manufacturing process, the resulting microstructure and the final properties, manufactured components have the potential to be further optimized with respect to both weight and performance, reducing their cost and environmental impact.



In his research, JOHAN JANSSON is interested in the description of materials using finite element methods. His focus lies on the development, implementation and evaluation of methods which enable a more accurate material description in structural simulations. Johan holds a Bachelor of Science in Mechanical Engineering, and a Master of Science in Product Development and Materials Engineering from Jönköping University.